Emergent $^1/_f$ noise in systems of oscillating nanomagnetic dots

A THESIS
SUBMITTED TO THE FACULTY OF THE GRADUATE SCHOOL
OF THE UNIVERSITY OF MINNESOTA
BY

Barry Nicholas Costanzi

IN PARTIAL FULFILLMENT OF THE REQUIREMENTS
FOR THE DEGREE OF
DOCTOR OF PHILOSOPHY

E. DAN DAHLBERG

August, 2016

Acknowledgements

No one makes it this far alone, and I am no exception; here I offer my thanks and gratitude to the many individuals who have helped me make it to where I am today. First and foremost, my adviser Dan Dahlberg. Dan's committment to his students above all else shows in both his advisory style, and his being a strong advocate for his students above all others. His advisement struck the perfect balance of offering direction while still allowing me to come into my own as an independent experimentalist, and really feel that I owned the work I did in the lab, embracing Herb Broida's decree (that was posted all over the lab) to make mistakes as quickly as possible to learn as quickly as possible. He also was always willing to go to bat for students over any University issue; knowing Dan was always in my corner was a huge help many times over.

The other graduate students in the Dahlberg lab–Tanner and Feng for showing me the ropes in my early days in the lab, Dan E and Bern for composing the other two-thirds of 'The St. Olaf Mafia" and being both imcomparably helpful peers, and great inspirations for the scientist I aspired to be, Dave for his unquenchable enthusiasm for grad school in the face of my increasing jadedness, and for being an unbelievably quick learner and indispensible lab mate, and James and Ben for injecting yet more new life into the lab, to carry on the maximization of JP products.

The members of the Goldman and Crowell labs, especially Terry, Tim, and Gordon, who were always willing to lend an outside perspective to any physics problem when necessary, and to help polish sack lunch and conference talks on their own time. Paul Crowell, whose tireless work and guidance made the move to the new building as painless as humanly possible–I can't think of a person I'd have rather had at the helm. Jon Kilgore and Bill Voje, for their instruction in the machine shop, helping me to efficiently and precisely machine experimental apparatus that I wouldn't have otherwise thought

myself capable of. The staff of the Minnesota Nanocenter, especially Bryan Cord and Kevin Roberts, whose unending and usually thankless efforts ensure that the world's most temperamental piece of equpiment, the Vistec EBPG 5000+, remains up and running for the countless grad students who rely on it. All of the administrative staff in the UMN Physics department, the unsung heroes without whom absolutely nothing would ever get done.

Carleton Urdahl, my high school math teacher, who first showed me the beauty of calculus and its applications, and who pushed and inspired me to look past the symbols on the paper to truly understand both their meaning, and their power. Amy Kolan, whose amazing intro mechanics class at St. Olaf showed me how much could be explained with so few equations, firmly cementing my love of physics. Jason Engbrecht, my undergrad research adviser, for introducing me to both my first taste of "real" scientific research, and to the joy of building useless contraptions in the Rube Goldberg contest. Melissa Eblen-Zayas, who took a chance on allowing me to teach a short intro course at Carleton College, giving me both the confidence in my own teaching and the experience on my resume to give me a springboard into pursuing a teaching career.

My family for always supporting me in all my endeavors, offering their unending encouragement even when they didn't really always understand just what I was doing. And to Kristen, my partner, whose emotional support through several of the most difficult years of my life cannot be overstated. I likely wouldn't be where I am today without her help, and her constant reminder that it's easy to feel dumb being surrounded by really smart people everyday, but that doesn't mean you are. Thank you for keeping me balanced and grounded.

In loving memory of Barry Vincent Costanzi, who was always my staunchest supporter and proudest fan.

Abstract

The observation of noise signals with a $\frac{1}{f}$ power spectral density dependence on frequency f is both ubiquitous in quantitative measurements across fields, and not entirely well understood. So-called "$\frac{1}{f}$" spectra have been observed in systems spanning the realm of physics, and in other disciplines as well. Van der Ziel's model of $\frac{1}{f}$ noise as a composite of Lorentizian noise signals is the most widely accepted explanation for $\frac{1}{f}$, but experiments have for the most part only implicitly confirmed the result thus far.

In this thesis, an explicit bottom-up approach to the Van der Ziel model is presented by combining random telegraph noise signals in square magnetic dots. Square dots made of the iron-nickel alloy Permalloy were fabricated to be 250 nm on a side and $\sim$ 10 nm thick. The configurational anisotropy of the dots is small enough to reduce energy barriers between adjacent magnetic states to approximately thermal energies through the application of an external field, causing two-state thermal hopping of the magnetization. This magnetization was measured through the anisotropic magnetoresistance of the dots. The random telegraph signals generate Lorentizan spectra when transformed to the frequency domain, and are shown to combine to form $\frac{1}{f}$ spectra when multiple dots are measured in series.

The energy landscape of the dots is determined through easy-axis coercivity measurements, and the distribution of energy barriers predicts a range of applied fields where individual noise signals should combine to produce $\frac{1}{f}$ noise by the Van der Ziel model. Experiment shows good agreement with the predicted range of these "noise fields" for two different series of samples with different coercivity distributions.

Measurements of both individual dots and aggregate multi-dot signals show that the number of individual oscillating dots necessary to produce an aggregate $\frac{1}{f}$ signal is lower than might be expected, with $\frac{1}{f}$ observed in collections of fewer than ten oscillating dots, and in some cases as few as two. Additionally, while the statistics over multiple samples agree with the Van der Ziel model, individual collections of dots exhibiting $\frac{1}{f}$ noise can either vary signifcantly from the ideal Van der Ziel distribution, or defy the distribution description altogether when the number of dots becomes too few. This suggests that the Van der Ziel model is a sufficient but not necessary condition for observing $\frac{1}{f}$ noise

in a collection of Lorentizan oscillators, and that the actual requirements to generate $\frac{1}{f}$ noise are much looser than Van der Ziel's. In systems with any type of distribution of Lorentizan signals, $\frac{1}{f}$ noise is likely due to combination of those signals. This result is relevant other systems exhibiting magnetic noise, as well as non-magnetic systems displaying both RTN and $\frac{1}{f}$ noise.

Contents

List of Tables

List of Figures

Chapter 1

Introduction

1.1 Why Study Noise?

Colloquially, the word "noise" usually indicates something both unwanted and unpleasant. The sound of a night train clattering by outside the window when one is trying to sleep, the din of sports fans trying to distract the opposing team's players; these "noises" serve only to obscure or annoy, and more importantly, are viewed as being *inherently devoid of content or worth.* There is no worthwhile information to be gleaned from listening more intently to the clanking of the train on the tracks or to the shouts of the home-team's fanbase. Noise is only suface-deep, and is innately useless; for most, it's just plain garbage.

So why study garbage? From a practical standpoint, perhaps understanding garbage is the first step to reducing it. Scientifically, noise is often also viewed as an obscuring signal to be avoided, but we can also gain insight into the source of these "garbage" signals by paying close attention to their content; by "listening" closely, we can understand their origins, and thus be able to more easily avoid them. Contrary to the earlier sentiment, noise viewed quantitatively actually contains important information, which can be used to damp out the sound of the train or ignore the jeers of the crowd more effectively.

From a purely academic standpoint, noise is rather interesting. "Noise" as a random signal is ubiquitous in any quantitative measurement on every scale, from measurements of quantum tunneling to population dynamics to cosmological observations. A naive

picture of random signals might conclude that there is nothing more to learn once a signal is deemed random, since by defintion randomness implies a strictly indeterministic phenomenon. However, a *statistical* analysis of random events can show patterns and features not present in any single random event, leading us to the somewhat unintuitive conclusion that these random processes are build upon rather rigid structures; underneath the chaos is order.

In this work, we examine the origins of so-called $\frac{1}{f}$ noise in systems of nanoscale magnetic square dots made of the nickel-iron alloy permalloy (Py) ($Ni_{80}Fe_{20}$). Magnetic noise is relatively understudied thus far, but has imporant consequences in many practical applications, especially in magnetic recording. Additionally, the underlying structure of $\frac{1}{f}$ noise has been implicitly examined experimentally before, but here we offer a more direct, ground-up demonstration of the emergence of $\frac{1}{f}$ from other constituent noise sources.

1.2 Overview

We give a brief introduction to the topic of noise in Chapter 1, and then develop much of the statistical and magnetic theory necessary to understand our experiments, described in Chapter 2. Chapter 3 gives a detailed overview of the experimental apparatus and methods, and the results of the experiment are reported in Chapter 4. We end with a look at unanswered questions and future work motivated by these experiments in Chapter 5.

Chapter 2

Theory

2.1 Noise

2.1.1 Definition of Noise

In most experiments, noise is defined as unwanted background signal, and much effort is typically given to reducing noise signals as much as possible so the signal of interest can be measured clearly. This defintion is rather subjective however; one can imagine a range of experiments where one experimenter's noise is another's signal. More objectively then, we define noise as any random or non-deterministic signal in a system. We can use the power spectral density, autocorrelation functions, time records, and other analytic methods to distinguish different types of noise. In this section, we define the characteristics used to differentiate noise signals before categorizing several different noise signals of interest.

2.1.2 Time Record

For a given noise signal, simply plotting its value as a function of time results in a *time record* measurement of the signal. Often the time records of different noise signals will not be obviously distinguishable, or at best will only appear qualitatively different. Typically the time record needs to undergo additional analysis to determine any quantitative information about the noise signal (an exception is Random Telegraph Noise, which will be discussed in section 2.2.3). The time record is in some senses, however,

the fundmamental element of the noise signal, since it is what is directly measured.

2.1.3 Autocorrelation function

Subjecting the time record to an *autocorrelation function* can uncover information on the dynamics of the noise signal and short term periodicity. For a given voltage (V) vs. time (t) record taken for a total time T, the autocorrelation function [1] as a function of time τ is

$$C_V(\tau) = \langle V(t)V(t+\tau)\rangle \tag{2.1}$$

where the expectation value is taken for all values of t such that both t and $t+\tau$ are $< T$. The autocorrelation function for a given value of τ can be understood as how much the signal at a given time t_0 is related to (or is *correlated* to) the signal a time τ later. For a stochastic signal, $C_V(\tau) \to 0$ as $\tau \to \infty$, but the way $C_V(\tau)$ decays to zero characterizes the noise signal.

2.1.4 Power Spectral Density (PSD)

Typically, the autocorrelation function is transformed to the frequency domain to understand its spectral content as a function of frequency f. This transformation gives the *power spectral density* or *PSD*, which is defined as

$$S_V(f) \equiv \int_0^\infty C_V(\tau)e^{-2i\pi f\tau}\ \mathrm{d}\tau \tag{2.2}$$

The PSD can be interpreted as indicating the power dissipated at a given frequency, and is how most noise signals are analyzed and distinguished from each other. We note here that though the most instructive way of interpreting the PSD is through relating it to the correlation function, for practicality the PSD is usually calculated from the average fourier transform of the time record; that is,

$$S_V(f) = \frac{\langle |v(f)|^2\rangle}{T} \qquad v(f) \equiv \int V(t)e^{-2i\pi ft}\ \mathrm{d}t \tag{2.3}$$

We present a detailed derivation of this result in appendix A. All experimental PSD figures in this work are produced by this method.

Total power dissipated can be calculated by integrating the PSD over all frequencies– clearly, this places a requirement on $S_V(f)$ to decay at a sufficient rate to prevent the

integral from diverging for the result to be physical. In general, arguments can be made to avoid high-frequency divergences based on scattering times, capacitive roll-offs, and other mechanisms [2, 3, 4]. However, general arguments to avoid low-frequency divergences (notably for spectra with $S_V(f) \propto f^{-1}$) are typically less robust [5]–we discuss this issue further in section 2.2.4.

We finally note that calculation of a PSD necessarily involves discarding any phase information about the signal, and thus a given PSD does not uniquely determine the time record of the signal the PSD was generated from. This point will be revisited in section 2.4.2, where we note that multiple magnetic processes may give similar PSDs, and only the time record data will allow a distinction to be made.

2.1.5 Unit and Notation Conventions

When dealing with stochastic voltage signals, it is often convenient to consider data in both the time and frequency domains. In the time domain, it is important to understand the size of background noise fluctuations so as to know the minimum observable measurement signal that can be seen above this "noise floor." For the common white noise floor (see section 2.2.1), the root-mean-squared (RMS) voltage fluctuations will be proportional to the square root of the bandwidth of the measurement, and so a white noise signal will often be described in units of $\frac{\mathrm{V}}{\sqrt{\mathrm{Hz}}}$ to make the RMS voltage noise easily calculable. This quantity is often not assigned a variable and is only referred to as the "noise floor" or "input noise"; when it is assigned a variable, it is commonly denoted as v_n [6].

As seen section 2.1.4, however, the typical frequency-domain measurement of PSD is in units of $\frac{\mathrm{V}^2}{\mathrm{Hz}}$. To make comparisons between domains easier, some adopt a convention of looking at what we will term the *voltage spectral density* (VSD), which is simply $\sqrt{\mathrm{PSD}}$, giving it the same units as the time-domain noise convention. (The VSD is also often convenient as it is proportional to the magnitude of the voltage signal in frequency space, which is easily seen from eq. (2.3)). Notation for this quantity does not seem to follow any specific convention, appearing sometimes as $N_V(f)$ or $e_n(f)$ [6]. Further complicating matters is that some engineering texts refer to a PSD whose signal units are in volts as a VSD, despite referring to a quantity with units of $\frac{V^2}{Hz}$.

The PSD at least, has one conventional notation in $S_V(f)$ when in units of $\frac{V^2}{Hz}$.

Unfortunately, the exception to this notation use appears to be in the work of Van der Ziel, upon whose noise theory much of this work relies; Van der Ziel variously notates the PSD as $F(f)$ [7] or as the traditional $S_V(f)$ [8], depending which work one refers to.

For clarity and consistency in this work, we will use the convention that all spectral densities in the frequency domain will be presented as *power* spectral densities in units of $\frac{V^2}{Hz}$ and notated as $S_V(f)$, and discussion of noise floors will always be in $\frac{V}{\sqrt{Hz}}$, and will be notated as v_n.

2.2 Types of Noise Signals

2.2.1 White Noise

In analogy to white light, whose frequency distribution is flat across the spectrum, *white noise* is a stochastic signal whose PSD is a constant value; that is, its fluctuations are frequency-independent, and thus are completely uncorrelated. A common example of white noise can be seen across an unbiased resistor. Thermal fluctuations of electrons in a resistor cause small, random voltage fluctuations called Johnson-Nyquist noise [9, 10]. For a resistor with resistance R at temperature T, the RMS voltage of fluctuations across the resistor is

$$V_{rms} = \sqrt{4k_B T R \Delta f} \tag{2.4}$$

where Δf is the bandwidth of the measurement. Consequently, this gives a noise floor value of

$$v_n = \sqrt{4k_B T R} \tag{2.5}$$

Due to the finite resistance in any electronic circuit, electronic equipment will also have finite values of white "input" noise that must be considered when calculating the expected noise floor of a given measurement. This combined white noise floor will set the minimum background PSD above which all other noise signals will be measured in this work. An example of white noise is shown in fig. 2.1(a)-(b).

2.2.2 Lorentzian ($1/f^2$) Noise

A *Lorentzian spectrum* is one of the form

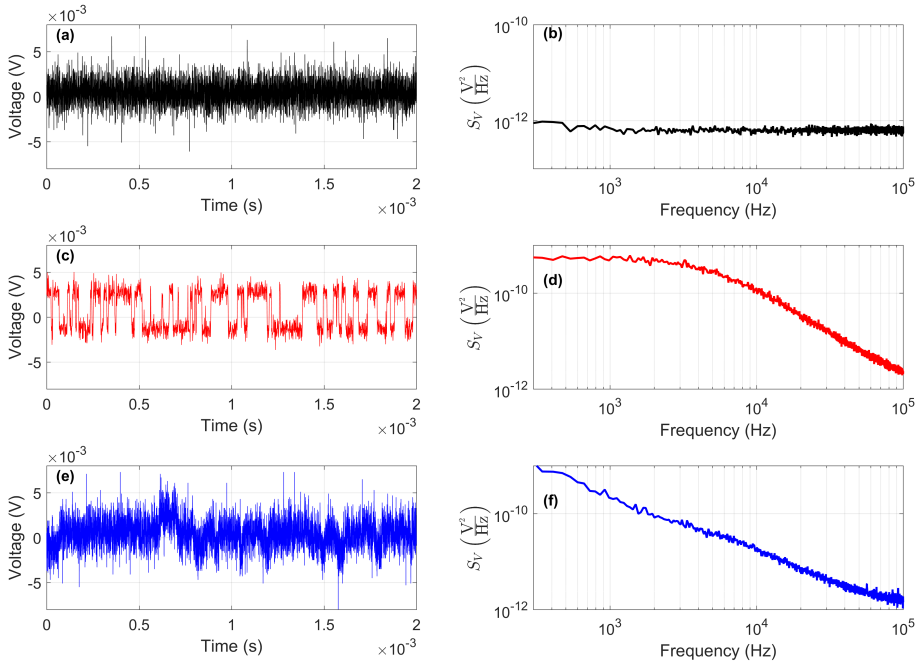

Figure 2.1: Time records and PSDs of serveral types of noise. White noise is shown in (a)-(b), characterized by its flat PSD. Random telegraph noise (RTN) is easily recognized by two-state switching in its time record, as seen in (c), which leads to the Lorentzian PSD shown in (d). A PSD showing $\frac{1}{f}$ noise with its logarithmic slope of -1 is shown in (f), with the corresponding time record shown in (e). We note that the time records shown strictly imply the corresponding PSDs, but the inverse is not true since phase information is lost in calculating the PSD from the time records.

$$S_V(f) \propto \frac{1/f_0}{1+(f/f_0)^2} \tag{2.6}$$

Shown in fig. 2.1(d), the noteworthy characteristics of the Lorentzian spectrum are a low-f frequency-independent region, appearing as a raised white noise floor, a high-frequency $\frac{1}{f^2}$ fall-off, and a "knee" at the characteristic frequency of f_0 where the white noise transistions to the high-frequency fall-off. This spectrum is often referred to as a $\frac{1}{f^2}$ spectrum due to its high-frequency behavior.

2.2.3 Random Telegraph Noise (RTN)

Also called "popcorn noise" or "burst noise", *random telegraph noise* (RTN) describes a two-state system whose switching probabilities are exponentially dependent on energy [2]. This two-state switching makes RTN one of the few stochastic signals which can be easily identified by its time record, displayed in fig. 2.1(c). To analyze RTN signals, we follow the procedure outlined in ref. [11]. For an RTN signal with the same probability to jump from state 1 to state 2 in a given amount of time as to jump from state 2 to state 1, the probability of n transitions occuring in a time τ is given by

$$P(n,\tau) = \frac{(\tau f_0)^n}{n!} e^{-\tau f_0} \tag{2.7}$$

where f_0 is the characteristic frequency of the transition. Suppose the system is electronic, with states 1 and 2 being voltages of $\pm V_0$. We calculate the autocorrelation function $C_V(\tau) = \langle V(t)V(t+\tau)\rangle$ of the voltage signal by noting that for an even (odd) number of transitions over a time interval τ, $V(t)V(t+\tau)$ must take the value $+V_0^2$ ($-V_0^2$). Thus,

$$C_V(\tau) = V_0^2 \left(P(n_e,\tau) - P(n_o,\tau)\right) \tag{2.8}$$

with

$$P(n_e,\tau) = \left(1 + \frac{(\tau f_0)^2}{2!} + \frac{(\tau f_0)^4}{4!} + \frac{(\tau f_0)^6}{6!} + \dots\right) e^{-\tau f_0} = \cosh(\tau f_0) e^{-\tau f_0} \tag{2.9}$$

$$P(n_o,\tau) = \left(\tau f_0 + \frac{(\tau f_0)^3}{3!} + \frac{(\tau f_0)^5}{5!} + \dots\right) e^{-\tau f_0} = \sinh(\tau f_0) e^{-\tau f_0} \tag{2.10}$$

Inserting eqs. (2.9) and (2.10) into eq. (2.8) gives

$$C_V(\tau) = V_0^2 e^{-\tau f_0} \left(\cosh(\tau f_0) - \sinh(\tau f_0)\right) = V_0^2 e^{-2\tau f_0} \tag{2.11}$$

A stochastic process should be even in time, however, so we can replace τ in eq. (2.11) with $|\tau|$, and then compute the PSD:

$$
\begin{aligned}
S_V(f) &= \int_{-\infty}^{\infty} C_V(\tau) e^{-2i\pi f\tau}\ d\tau \\
&= V_0^2 \int_{-\infty}^{\infty} e^{-2|\tau| f_0} e^{-2i\pi f\tau}\ d\tau \\
&= V_0^2 \left(\int_{-\infty}^{0} e^{\tau(2f_0 - 2i\pi f)}\ d\tau + \int_{0}^{\infty} e^{-\tau(2f_0 + 2i\pi f)}\ d\tau \right) \\
&= V_0^2 \left(\frac{1}{2f_0 + 2i\pi f} + \frac{1}{2f_0 - 2i\pi f} \right) \\
&= V_0^2 \frac{f_0}{f_0^2 + \pi^2 f^2}
\end{aligned}
\tag{2.12}
$$

This PSD is of the form of eq. (2.6), and thus we see that the equally weighted RTN system has a Lorentzian PSD.

In general, an RTN system's switching probabilities will not be symmetric, as we assumed above. However, it can be shown that for an assymetric RTN system with switching rates f_{12} and f_{21}, the PSD will again be Lorentzian, with roll-off occurring at the average frequency $\frac{f_{12}+f_{21}}{2}$ [12]. Thus, we have the general result that all RTN signals have Lorentzian PSDs.

2.2.4 $1/f$ Noise

Also known as *flicker noise*, $\frac{1}{f}$ *noise* gets its name from its PSD frequency dependence, though we note that the convention of what spectral exponents actually "count" as $\frac{1}{f}$ is a little loose; exponents ranging anywhere from -0.7 to -1.3 are categorized as "$\frac{1}{f}$" [11]. An example of $\frac{1}{f}$ noise in both the time and frequency domains is shown in fig. 2.1(e)-(f). This type of spectrum is notable for both its ubiquity, and for the lack of a consistent theory to explain its appearance in many seemingly disparate systems; $\frac{1}{f}$ has been reported in systems ranging from voltage measurements in electronic systems [5, 11, 13], quasar intensity [14], neuron firing events [15], and flood levels of the Nile [16], just to name a few. Various magnetic systems [17, 18, 19] have also shown $\frac{1}{f}$ spectra.

Various theories have been proposed to explain $\frac{1}{f}$ noise, with varying degrees of generality. Narrower $\frac{1}{f}$ theories typically focus on voltage noise seen in semiconductor

systems. For such electronic systems, proposed theories suggest mechanisms of mobility fluctuations [20], fractional order integration [21], and bremsstrahlung radiation of carriers [22]. Perhaps the most general theory to explain $\frac{1}{f}$ noise, though, is Van der Ziel's observation that $\frac{1}{f}$ can be constructed from a distribution of Lorentzian spectra [7]; we explore this idea in detail in section 2.2.5.

Further problems with $\frac{1}{f}$ spectra arise from their divergent integrated power. For a $\frac{1}{f}$ spectrum, total dissipated power over a bandwidth $\Delta f = f_2 - f_1$ is

$$P \propto \int_{f_1}^{f_2} \frac{\mathrm{d}f}{f} = \ln(f_2/f_1) \tag{2.13}$$

From this expression, we can see that the total diverges for both $f_1 \to 0$ and for $f_2 \to \infty$. The high-f divergence problem can be mitigated in a real physical system by the arguments mentioned in section 2.1.4, but the low-f divergence is more problematic. One can postulate that a low-frequency roll-off must occur at some point, but the lowest frequency measurement in semiconductors thus far ($10^{-6.3}$ Hz) [23] showed no sign of such a roll-off. The commonly accepted workaround to this problem is to note that, given the age of the universe is 10^{17} s, the lowest meaningful frequency one could possibly integrate from is 10^{-17} Hz (and since no real sample is as old as the universe, practically speaking this value could be increased by several orders of magnitude). This imposes a practical frequency limit on such calculations, which recovers a finite total power value [24]. This workaround appears to relegate the low-frequency divergence problem to only a mathematical problem, and not a physical one. (We note also that Ref. [24] also makes a physical argument for a high-frequency limit in electronic systems based on atomic length scales and a speed limit of c, rather than assuming a high-frequency capacitive roll-off mentioned in section 2.1.4.)

2.2.5 Emergent $1/f$ Noise from Ensembles of $1/f^2$ Signals (Van der Ziel Theory)

Here we recreate Van der Ziel's theory to explain $\frac{1}{f}$ noise [7], which begins with the general idea of an ensemble of relaxing systems characterized by relaxation times τ_r and which all have PSDs of the same form $S_V(f, \tau_r)$. If the ensemble has a distribution of relaxation times $g(\tau_r)$, then the total PSD of the composite system will be

$$S_V(f) = \int_0^\infty S_V(f, \tau_r) g(\tau_r)\ d\tau_r. \tag{2.14}$$

In principle, then, for a given $S_V(f, \tau_r)$, an ad hoc choice of $g(\tau_r)$ can always be made to yield $S_V(f) \propto \frac{1}{f}$. The physicality of $g(\tau_r)$, is not at all guaranteed, however– the physical validity of the theory depends on the plausibility of the choice of $g(\tau_r)$.

If we consider a distribution of Lorentzian spectra as in eq. (2.6), and let $f_0 = 1/\tau_r$, so that

$$S_V(f, \tau_r) \propto \frac{\tau_r}{1 + (\tau_r f)^2} \tag{2.15}$$

we can choose a distribution function

$$g(\tau_r)\ d\tau_r = \begin{cases} C\frac{d\tau_r}{\tau_r} & \tau_1 \leq \tau_r \leq \tau_2 \\ 0 & \text{elsewhere} \end{cases} \tag{2.16}$$

where C is a constant. This distribution then gives a total PSD of

$$\begin{aligned} S_V(f) &\propto \int_{\tau_1}^{\tau_2} \frac{\tau_r}{1 + (\tau_r f)^2} \frac{d\tau_r}{\tau_r} \\ &= \frac{\left(\tan^{-1}(\tau_2 f) - \tan^{-1}(\tau_1 f)\right)}{f} \end{aligned} \tag{2.17}$$

We note that $\tan^{-1}(\tau_2 f) \approx \frac{\pi}{2}$ for $f \gg 1/\tau_2$, and $\tan^{-1}(\tau_1 f) \approx 0$ for $f \ll 1/\tau_1$. Thus, the result of eq. (2.17) gives a spectrum that goes as $\frac{1}{f}$ in the region $1/\tau_2 \ll f \ll 1/\tau_1$, as illustrated in fig. 2.2.

To evaluate whether $g(\tau_r)\ d\tau_r = C\frac{\mathrm{d}\tau_r}{\tau_r}$ is physically plausible, we consider a thermally activated process, such that the relaxation time is described by

$$\tau_r = \tau_0 e^{\Delta E/kT} \tag{2.18}$$

where τ_0 is some attempt frequency, and ΔE is the energy barrier associated with the transistion. Taking a differential of each side of eq. (2.18) and then dividing both sides by eq. (2.18) gives

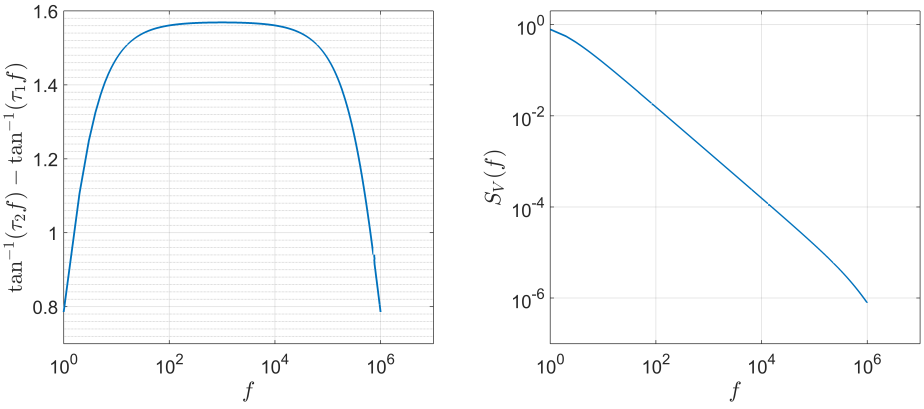

Figure 2.2: Plots of the numerator of the result from eq. (2.17), as well as the full result. Values of $\tau_1 = 1$ s and $\tau_2 = 10^{-6}$ s are used to produce (a). The value of the function is nearly constant for all values of f at least an order of magnitude greater than $1/\tau_1$ and and order of magnitude less than $1/\tau_2$. This leads to the full term describing $S_V(f)$ being proportional to $\frac{1}{f}$ for the majority of frequency space shown, as in (b).

$$g(\tau_r)\, d\tau_r \propto \frac{d\tau_r}{\tau_r} = \frac{d\Delta E}{kT} \propto g(\Delta E)\, d\Delta E \tag{2.19}$$

Thus we require a flat distribution of energy barriers over the range $E_1 > \Delta E > E_2$ to achieve a $\frac{1}{f}$ distribution.[1] We will examine this requirement in more detail in section 2.4, but we note here that in general, this is not an overly restrictive requirement, as the exponential dependence of τ_r on ΔE means that even a small energy spread $E_1 - E_2$ will result in a large spread of τ_r's in eq. (2.16).

2.3 Magnetic Energies and Anisotropy

In a given ferromagnet, the magnetic configuration is the result of a number of competing energies, which may include both internal self energies of the magnet, and external agents like applied fields or mechanical stress. Minimization of these energies will typically cause the magnetization to point in certain directions in the sample; due to this symmetry breaking, these energies are often called *anisotropies*. The intrinsic energies

[1] Work by ref. [25] has shown that this requirement is likely overly restrictive, and that any reasonably well-behaved distribution of barriers will lead to $\frac{1}{f}$ noise. For simplicity, however, we will proceed with the flat distribution picture.

that can give rise to this anisotropy are the exchange energy, the dipole-dipole interactions often referred to as demagnetization or magnetostatic energy, and the crystalline anisotropy energy. In what follows, we discuss the roles these magnetic energies play in determining the full energy landscape of the system, as it is the thermal fluctuations over barriers in the energy landscape that lead to the magnetic noise later described in section 2.4.

2.3.1 Zeeman Energy

We begin with the simplest energy in a ferromagnetic system, the externally induced *Zeeman energy*. A magnetic moment $\mathbf{m}$ in an externally applied field $\mathbf{H}$ is described by an energy

$$E = -\mathbf{m} \cdot \mathbf{H} \tag{2.20}$$

This Zeeman energy is the most common way to control the magnetization of a ferromagnetic sample.

2.3.2 Exchange

Exchange is a quantum mechanical effect that is the overall reason for non-zero remnance magnetization in any ferromagnet. Exchange is a consequence of the Pauli exclusion principle, which states that no two fermions can have the same set of quantum numbers at the same time. For electrons, this is typically taken to mean that electrons cannot have the same spin and same orbital state. Valence electrons with the same spin state in different orbitals minimize their spatial overlap, and consequently reduce electrostatic repulsion between the electrons. In certain materials, this interaction dominates over the magnetostatic energy described in section 2.3.3, leading to an ensemble of parallel spins, and ferromagnetism. Further details on the exchange interaction can be found in Refs. [26, 27]–for the purposes of this work, it suffices to say that the exchange interaction is a short range interaction that can be approximated to only act between nearest neighbors in a lattice, making exchange an intrinsic effect.

2.3.3 Demag Fields and Shape Anisotropy

If one considers the classical picture of a ferromagnet as simply a collection of individual moments or spins, it is easy to show that any given spin will be subjected to an internal magnetic field created by the remaining spins–this is known as a demagnetizing or *"demag" field* since the net field will point in the opposite direction to the net magnetization. We label this field $\mathbf{H_d}$. This demag field results in an increase in internal Zeeman energy (see eq. (2.20)) due to its interaction with the local magnetization, which the system will attempt to minimize by altering its magnetic state. A simple qualitative analysis as shown in fig. 2.3 leads to the conclusion that ferromagnets will prefer magnetization to point along the longest axis of the ferromagnet.

We also present a more rigorous quantitative analysis of the magnetostatic energy. By supposing that there are no internal currents in the sample, and imposing the boundary condition that $\mathbf{M} = 0$ outside the sample, the magnetostatic Poisson equation $\nabla^2 \Phi_M = -\nabla \cdot \mathbf{M}$ can be solved, and then $\mathbf{H} = -\nabla \Phi_M$ can be calculated [27, 28] to find

$$\mathbf{H_d}(\mathbf{r}) = -\frac{1}{4\pi} \int_V \frac{\nabla' \cdot \mathbf{M}}{|\mathbf{r} - \mathbf{r}'|^2} \hat{\mathbf{r}} \, \mathrm{d}^3\mathbf{r}' + \frac{1}{4\pi} \int_S \frac{\mathbf{n}' \cdot \mathbf{M}}{|\mathbf{r} - \mathbf{r}'|^2} \hat{\mathbf{r}} \, \mathrm{d}^2\mathbf{r}' \tag{2.21}$$

where we have suppressed the argument of $\mathbf{M}(\mathbf{r}')$, and where $\hat{\mathbf{r}} \equiv (\mathbf{r} - \mathbf{r}')/|\mathbf{r} - \mathbf{r}'|$.

In the simplest case of a material with uniform magnetization (so $\nabla' \cdot \mathbf{M} = 0$), the volume integral vanishes and we are left only with the surface term. This term depends only on the magnetization normal to the surfaces, so to minimize the term, the sample will try to point $\mathbf{M}$ parallel to its surface, agreeing with our qualitative picture described above. This effect becomes especially apparent with samples with a high aspect ratio; for obvious reasons, this effect is also known as *shape anisotropy*.

In general, ferromagnets will not have a uniform $\mathbf{M}$ due to the competition between the intrinsic exchange energy (which prefers uniform $\mathbf{M}$) and the extrinsic magnetostatic energy (which prefers to form domains to make $\mathbf{M} \cdot \hat{\mathbf{n}} = 0$). (This is to say nothing of other anisotropies in the system, which could further complicate things.) This competition leads to a length scale called the *exchange length* l_e, which denotes the typical size of domain walls in a sample [27]. This competition also leads to samples of smaller dimension being more likely to exhibit a single-domain configuration than larger ones.

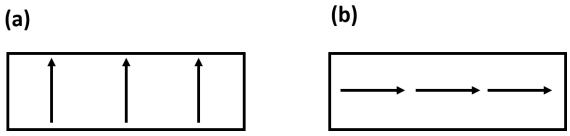

Figure 2.3: A cartoon of a high- and low-energy state of a rectangular ferromagnet with a large aspect ratio. Since all the spins are aligned in both (a) and (b), the exchange energy for both is equal, but in (a) the demag field produced by any given spin is anti-parallel to all the other spins in the magnet, making the Zeeman energy a maximum. In (b), demag fields align with other spins, minimizing the Zeeman energy. Thus the magnetization prefers to point along the long axis of the ferromagnet, as in (b).

2.3.4 Crystalline Anisotropy

In some materials, the crystalline structure of the material can also introduce preferred magnetization directions as a consequence of spin-orbit coupling. Briefly, the orientations of electronic orbitals are coupled very strongly to the crystallographic directions of the lattice, and the spin of the electron is weakly coupled to the orbital direction, and thus the spin ends up weakly coupled to the lattice [26]. This is known as *crystalline anisotropy*. It is worth noting that a sample need not be a single crystal to exhibit crystalline anisotropy, as most polycrystalline samples have at least some preferred orientation of the crystallites, leading to a much weaker (but non-zero) crystalline anisotropy.

In the work presented in this thesis, permalloy was chosen for its extremely low crystalline anisotropy–due to both permalloy's small crystalline anisotropy, and the polycrystallinity of our samples, it can be assumed that the crystal anisotropy of our samples is negligible.

2.3.5 Configurational Anisotropy

As noted in section 2.3.3, shape anisotropy is most relevant in samples with large aspect ratios. In more symmetric samples, however, the shape anisotropy term can become isotropic, necessitating the more microscopic picture of *configurational anisotropy* [29]. In thin film square dots, for example, it is clear that shape anisotropy will prefer $\mathbf{M}$ to be in the plane of the dot, but it can be shown that the shape anisotropy term becomes

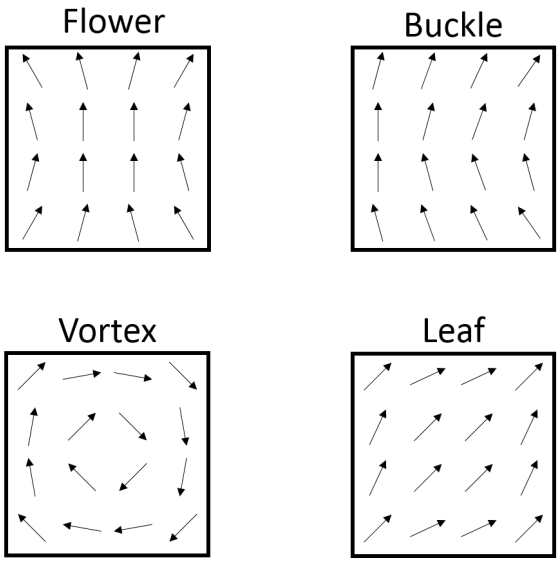

Figure 2.4: Cartoon showing the four magnetic configurations in permalloy dots proposed by [31]. A given dot will assume the zero-field ground state that minimizes its total magnetic energy. The ground state will be determined by the dot dimensions. Transport measurements like those in ref. [32] show that the dots in this work have a ground state with net magnetization pointed along the edge of the dot, and thus are in either the "buckle" or "flower" state.

equal in all directions in the plane [30]. A larger dot may then adopt a multidomain structure to minimize its energy, but if the dot is small enough it may instead adopt more nuanced magnetic state. For instance, one can imagine that a slightly curved or C-shaped magnetization configuration in the dot could reduce magnetostatic energy, and if the sample is large enough so that the curving is gradual, the gain in exchange energy may be small enough for the dot to favor the curved state over a uniform magnetization. Simulations by Cowburn, et. al [31] of permalloy dots show that any of four different magnetization ground states can arise depending on side length and thickness.

Previous work in our lab has characterized dots presumed to be in either the "buckle" or "flower" state shown in fig. 2.4 [32], and has shown that dots exhibiting this ground state can be described by a four-fold symmetric configurational anisotropy that prefers

the *net* magnetization of the dot to point along one of the dot edges. Using the Stoner-Wohlfarth picture [33] to track the *net* direction of the magnetization, we model this configurational anisotropy as a function of magnetization direction θ as

$$E(\theta) = -\frac{E_A}{2}\cos(4\theta) \tag{2.22}$$

where E_A can be interpreted as the difference in energy between $\mathbf{M}$ pointing along a diagonal of the dot versus $\mathbf{M}$ parallel to the edge of the dot in zero applied field.

2.4 Magnetic Noise

Most ferromagnetic systems have a magnetization that can be considered fixed for a given set of static conditions due to anisotropy. However, since the energy barriers between magnetization states are extrinsic quantities, by sufficiently reducing the volume of the dot, a barrier size can be reached where application of an external field can reduce the barrier height to near thermal energies, causing thermally activated switching of the magnetization [32, 34, 35]. Traditional magnetometry techniques cannot measure the magnetization in such a small volume, but magnetoresistance effects can be used to determine magnetization from transport measurements. Here we describe both the magnetoresistance effect used to detect magnetic noise, and the theory behind random telegraph noise that is measured in magnetic dots.

2.4.1 Anisotropic Magnetoresistance (AMR)

In a ferromagnetic material, the resistance of the material can be shown to depend on the angle between the current and the net magnetization; this is called *anisotropic magnetoresistance* (AMR). A detailed description of AMR is beyond the scope of this work, but in brief, spin-orbit coupling in a ferromagnet causes an anisotropy in the scattering cross-section between conduction electrons and d-orbital electrons in the material, causing certain directions to have lower resistance than others [36]. Phenomenologically, the AMR is given as

$$R(\theta) = R_0 + R_1\cos^2\theta \tag{2.23}$$

where θ is the angle between the magnetization and the current, R_0 is the resistance for current and magnetization perpendicular, and R_1 is the difference in resistance between the parallel and perpendicular states. The sign of R_1 is material dependent, but is typically a positive quantity. In permalloy specifically, $R_1 > 0$, meaning that $I \parallel M$ gives a resistance maximum, and $I \perp M$ gives a resistance minimum. Thus, the AMR can be used to determine a sample's net magnetization up to a factor of π, and if something is known about the sample's magnetic history (usually due to some past application of a saturating field), the net magnetization can be completely determined by transport measurements.

We note here that, though our samples do not have a uniform **M** ground state (as detailed in section 2.3.5), the *net* magnetization between orientations of the buckle state are large enough that the difference between the two are easily distinguished using AMR.

We also proceed with the convention that current will always flow in what is defined as the positive x-direction through the dots, so that θ above can be defined simply as the direction of the magnetization, without loss of generality.

2.4.2 Magnetic RTN

Previous work has shown that the magnitude of the configurational anisotropy can be tuned by varying the side length of dots [32]. Tuning the energy barriers in combination with the application of an external field along the diagonal of the dot can reduce the total energy barrier to be on the order of themal energies. In this case the magnetization will undergo activated switching between states [34]. Quantitatively, for an applied field of strength H at an angle ϕ to the horizontal, we can express the total energy landscape in this situation as

$$E(\theta) = -\frac{E_A}{2}\cos(4\theta) - mH\cos(\theta - \phi). \tag{2.24}$$

For no applied field, energy barriers between minima will be too high for switching as shown in fig. 2.5(a), so magnetization should remain constant. Two state switching will be observed when the total height of the energy barrier between wells is comparable to thermal energy k_BT. If we assume that the dot magnetization minima remain at 0°

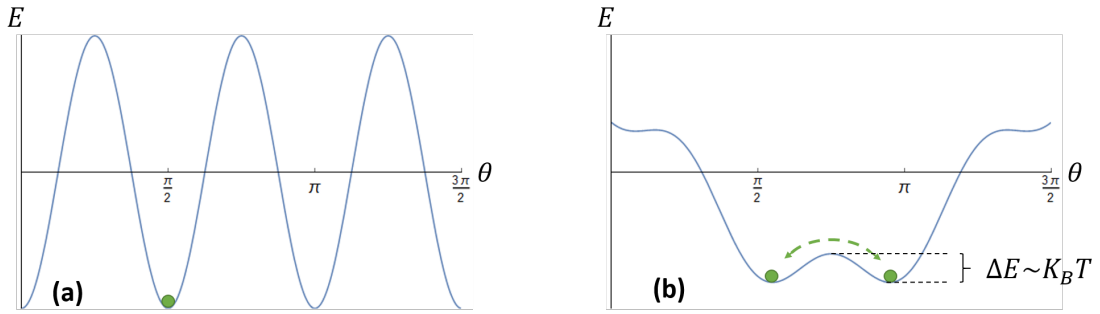

Figure 2.5: Plots of the combined energy landscape E as a function of magnetization angle θ for both zero applied field (a), and for a field applied at $\phi = \frac{\pi}{4}$, calculated from eq. (2.24). The green ball represents the direction of magnetization. In (a), energy barriers between wells are much too high for switching to occur, but in (b), for the right applied field strength, the barrier between wells will be low enough that the magnetization can thermally jump between two minima. This jumping can be detected in the AMR signal.

and 90° to the dot horizontal and that the applied field is along the diagonal of the dot, then the height of the energy barrier is

$$\begin{aligned} \Delta E &= E(\frac{\pi}{4}) - E(0) \\ &= E_A - mH\left(\frac{2-\sqrt{2}}{2}\right). \end{aligned} \tag{2.25}$$

So for $\Delta E \approx k_B T$ as shown in fig. 2.5(b), the magnetization should undergo thermal hopping. If the two states have net magnetization that are at different net angles θ to an applied current in the dot, this hopping can be observed through the AMR.

For identical dots, any given dot should undergo RTN at the same characteristic frequency for a given applied field strength H and angle ϕ. However, due to fabrication imperfections (rounded corners, granular structure, etc.), "identically" fabricated dots will vary slightly in structure, and so collections of such dots will have a range of effective energy barriers for a given (H, ϕ), and thus a range of characteristic frequencies, as expected from eq. (2.18). Given the arguments made in section 2.2.5, if a collection of oscillating dots is measured at the same time, $\frac{1}{f}$ could be observed.

We briefly note previous work showing that relaxation processes in magnetic systems

can also give PSDs with spectral exponents between -1 and -2, which can mistakenly be categorized as noise if only the PSD is examined [37, 38]. Consequently, any work on magnetic noise must prioritize both PSD measurements *and* time record data, since only the time record gives unambiguous confirmation about whether the PSD is due to stochastic signals or relaxation processes.

Chapter 3

Experimental Methods

3.1 Sample Fabrication

All samples were fabricated using a combination of tools in the Minnesota Nanocenter (MNC) and an in-house UHV sputtering system. Materials were patterned and deposited on a insulating substrate of 500 nm of CVD-deposited amorphous Si_3N_4 on top of 1 mm of silicon; the substrates were produced by NVE corporation. Patterning of samples involved three discrete lithography steps, including an optical lithography step to define coarse Au contacts, and two electron beam lithography steps to define both the Py dots and the small Au contacts that connect to the dot.

3.1.1 Sample geometry

An overhead cartoon view of the sample chip at various magnifications is shown in fig. 3.1. The 250 nm magnetic square dots can be seen in fig. 3.1(e) in blue, with the Au vias linking adjacent dots together in pink and green (the different colors represent different electron-beam write steps; see section 3.1.5). These vias connect to the photolithographically patterned Au contact pads in red (see section 3.1.4). The 16 contact pads seen in fig. 3.1(b) allow wire bond connections between the sample and the sample mount, in order to source current through the dot chain, and to measure voltages across dots; a zoomed in image is shown in fig. 3.2. Dots are patterned in an array with 1 μm spacing between dot centers; clearly only a small fraction of the patterned dots is actually measured, but the array pattern was chosen to ensure any magnetostatic coupling

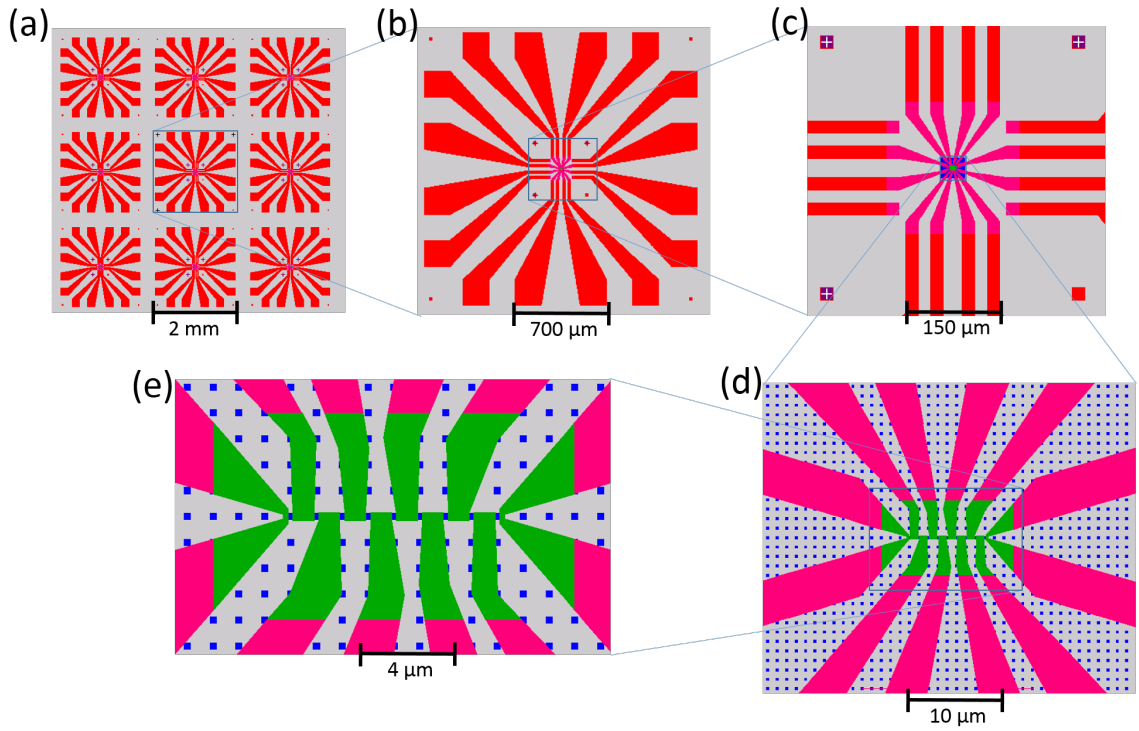

Figure 3.1: Overhead CAD images of sample geometry, with increasing magnification moving from (a) to (e). Red, pink, and green regions represent Au conducting vias, while the small blue squares represent the magnetic dots. (a) shows the nine measurement areas patterned on a single chip, (b) shows a single area, and (c)-(e) show various levels of increasing magnification of a single area.

between dots was uniform for any dot on the chain.

3.1.2 Materials

In fig. 3.1, both the coarse contacts in red and the fine contacts in pink and green are deposited as a thin seed layer of some transition metal with a thicker layer of Au on top. Gold is desired for vias due to both its high conductivity and its resistance to corrosion; this ensures that the resistance of the vias is low, making the Johnson-noise floor (see section 2.2.1) low and the experiment sensitive to small signals. The transition metal seed layer is necessary to promote adhesion to the Si_3N_4 substrate, as Au's adhesion to insulators is very poor.

Figure 3.2: A close-up cartoon of the sample geometry. Pink areas represent the W/Au contacts, and yellow areas represent the magnetic dots. With this geometry, current can be sourced through the ends on the contacts marked I+ and I-, and then any other pair of contacts can be chosen as voltage contacts to measure any combination of adjacent dots simultanously.

For the coarse contacts, a structure of 30 nm Ti / 170 nm Au is deposited by thermal evaporation, with Ti chosen as a seed layer for its ease of deposition. For the fine contacts, a thinner structure of 5 nm W / 15 nm Au is deposited by sputtering; early iterations of the experiment used evaporated Ti as the seed layer, but after several hours of measurement, Py dots displayed irreversable degradation of magnetic properties including reduction of remnance magnetization (as measured by AMR), and loss of well-defined coercivity. We posit that this is due to Ti electromigrating into the Py dot, as Ti is already known to thermally diffuse into Py rather easily [39]. After switching the seed layer to W, which diffuses in Py far less readily [40], this problem is no longer observed.

The magnetic dot consists of a 3 nm seed layer of Ta (once again to promote adhesion to the substrate), a 10 nm layer of Py, and a 3 nm capping layer of Ru. Permalloy was

chosen as the magnetic material due to its low crystalline anisotropy and its high AMR. The capping layer prevents oxidation of the Py, and Ru is chosen in particular due to its oxide being a conductor, which reduces contact resistance between the dot and the contacts, helping minimize Johnson-Nyquist noise (see section 2.2.1).

3.1.3 Substrate Preparation

Prior to any given lithography step, samples are cleaned in a solvent rinse sequence of Acetone → Methanol → Isopropanol, ensuring at each step that the previous solvent is fully removed to avoid residue. Substrates are then dried using a N_2 gun and then baked on a 180° C hot plate for 10 minutes to ensure no liquid remains adsorbed to the substrate, which can create problems for resist adhesion.

3.1.4 Photolithography

Photolithographic patterning is a convenient lithography technique when the same pattern is to be used many times, and when feature scales are not too small (∼1 um or larger). A reusable glass "mask" is patterned with opaque chrome to be used as a window for UV light to be exposed onto a substrate coated with a UV-sensitive polymer called photoresist. The exposure process transfers the pattern on the mask to the substrate via the UV light. This process is quick and inexpensive, but comes at the cost of flexibility in patterning; if a new pattern is desired, a new mask must be fabricated. Throughput is very high, however; unlike a process like electron-beam lithography (described in section 3.1.5), whose process length scales with size, photolithographic process time-scales are effectively size-independent.

In this work, photolithography is used to define the wire-bonding pads on each sample chip, as well as large-scale vias leading to the center of each chip. An unpatterned Si_3N_4/Si wafer is first spin-coated at 3000 rpm for 30 s with 350 nm of Microchem LOR-3A resist, then baked on a 170°C hot plate for 5 minutes. After cooling, a 500 nm thick layer of Shipley Microposit S1805 photoresist is spun on to the wafer by spinning at 3000 rpm for 30 s, which is then baked for 115°C for 2 minutes.

The coated wafer is then patterned in either a Karl Suss MA6 or MABA6 contact aligner. A chrome photomask is placed above the wafer, and the photoaligner is run in

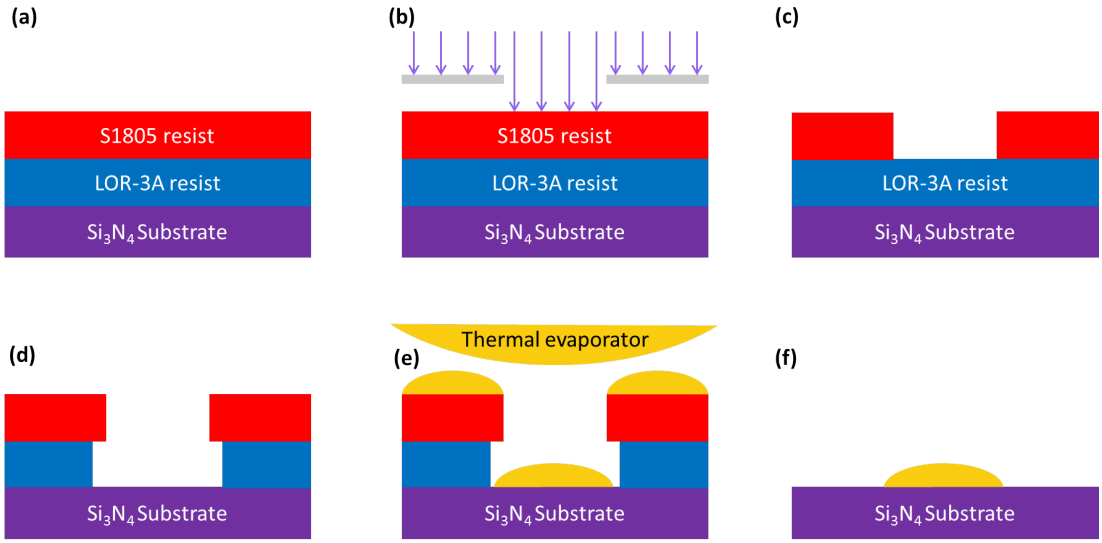

Figure 3.3: A cartoon showing a side view of the fabrication of the coarse Au contacts (not to scale). The substrate is spin coated in a layer of LOR-3A resist, and then a layer of S1805, as in (a). The substrate is then exposed to UV light through a photomask shown in (b), making the exposed S1805 soluble in developer. The photomask pattern is dissolved out of the S1805 layer, creating the patterned hole shown in (c). The second development step dissolves the LOR-3A isotropically; waiting a short time after the resist has dissolved down to the substrate produces the horizontal undercut shown in (d). A directional depositon method such as thermal evaporation shown in (e) produces little to no fencing after liftoff, as seen in (f).

soft-contact mode with a 20 μm exposure gap. A 350 watt UV ($\lambda =$ 350 nm - 450 nm) lamp is illuminated for 2.5 s, exposing those areas of the wafer underneath the clear parts of the photomask and transferring the photomask pattern to the resist.

The exposed resist is now highly soluable in a photoresist developer, and so the wafer is submerged in a 1:5 solution of Microposit 351 Developer : H_20 for 25 s to develop the S1805 layer. The wafer is then baked again at 125°C for 5 minutes to "hard-bake" the remaining S1805 to prevent further development. The LOR-3A layer is then developed for 60 s in the TMAH-based Microposit MF CD-26 developer to create the "undercut" as shown in fig. 3.3.

A sequence of 30 nm Ti / 170 nm Au are deposited in a CHA Thermal evaporator, after which a liftoff process is performed in a 1:1 mixture of Acetone : N-Methyl-2-pyrrolidone (NMP). Liftoff can take as little at 1 hour, but is usually done overnight.

The wafer is then washed in the same solvent sequence as in section 3.1.3, and is coated again with a single layer of thick (1.8 μm) Shipley S1818 photoresist to protect it from debris while dicing.

The wafer is then diced into 9.8 mm x 9.8 mm square chips using a Disco DAD 2H/6T wafer saw. We note that, despite the mask pattern having a period of 10 mm across the wafer, the chips are diced to be slightly smaller than 10 mm x 10 mm so they more easily can be inserted and removed from the 10 mm x 10 mm recess in the DIP chips described in section 3.2.1. This does, however, introduce some uncertainty in the field angle with respect to the chip during measurement.

3.1.5 Electron-beam Lithography

The fundamental limitations of photolithography are resolution limits set by the exposure wavelength λ (due to diffraction smearing sub-λ features in a mask), and difficulty in making iterative changes to a pattern since a new mask must be produced for each new desired pattern. Electron-beam lithography (EBL) overcomes both these limitations, at the cost of a more time-intensive patterning process. In EBL, an exposure pattern is "drawn" onto a resist-coated substrate by a highly focused electron beam. Since the wavelength of an resting electron is much smaller than UV light (and accelerating the electron will lower the wavelength further), EBL is capable of writing much smaller features than photolithography. (We note that in practice, EBL resolution is typically not set by wavelength, but by beam coherence/spot size, electron beam backscatter, and the polymer structure of the resist used, but this still affords a resolution of $\sim$10 nm, which beats photolithography by several orders of magnitude.) Since EBL patterns are all software based, this also makes for easy prototyping and iterative adjustments to patterns. As noted, this comes at the cost of a longer patterning process; judicious choice of beam currents and spot sizes can minimize write times, but depending on pattern resolution and complexity, EBL writes can take anywhere from minutes to days.

EBL is used twice for each sample prepared in this work. First, individual chips produced in section 3.1.4 are spin-coated at 5000 rpm with a resin of 2% poly(methyl methacrylate) in chlorobenzene (PMMA-C2) to a thickness of $\sim$100 nm, as shown in fig. 3.4(a). The resist is baked on a hotplate at 180° C for 5 minutes, and then dots are patterned in a Vistec EPBG 5000+ EBL system. After development in a 3:1 solution

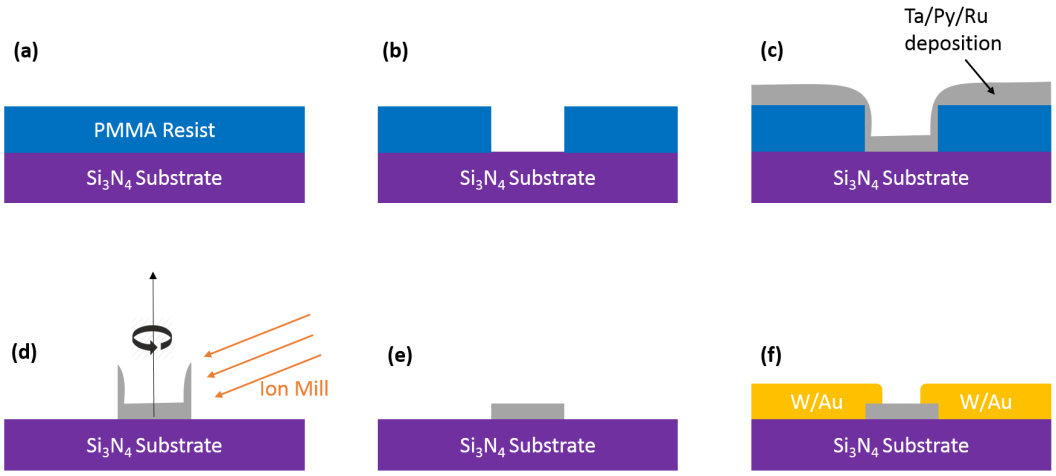

Figure 3.4: A cartoon showing a side view of the fabrication of dots and fine contacts (not to scale). PMMA resist is spun onto the substrate as in (a), and is then patterned by EBL and developed to give the resist profile in (b). Sputtering of the magnetic dots results in (c), and after liftoff dots with fencing as shown in (d) are left. During the ion mill step, the sample rotates about the vertical axis of the picture to ensure that fencing on all sides of the dot is removed, resulting in the dot shown in (e). A similar sequence of steps results in the deposition of the W/Au contacts shown in (f).

of isopropanol:methyl isobutyl ketone (MIBK), dots are deposited as described in section 3.1.6; these steps are illustrated in fig. 3.4(b)-(c). Liftoff is performed in the same acetone:NMP solution as in section 3.1.4, resulting is the structure shown in fig. 3.4(d).

The single-layer resist used for patterning the dots results in a higher resolution (most notably, sharper corners) than if a bi-layer recipe were used, but the liftoff creates fencing on the edges of the dot. Since these large narrow features could introduce unwanted shape anisotropy and pinning sites to the dots, an oblique (15° to the plane of the chip) ion mill step in an Intlvac Nanoquest Ion Mill is used to remove the fencing; fig. 3.4(d)-(e) illustrate this process, with the results on real samples shown in fig. 3.5(c). Deposition parameters for sputtering were also chosen to help avoid fencing as much as possible–we discuss this in more detail in section 3.1.6.

Once the dots are patterned, the chip undergoes a second EBL process, this time using PMMA-C4 spun to ∼200 nm thickness, to pattern electrical contacts to the strings of dots. After development, the sample is submitted to a brief ion mill step at an incident

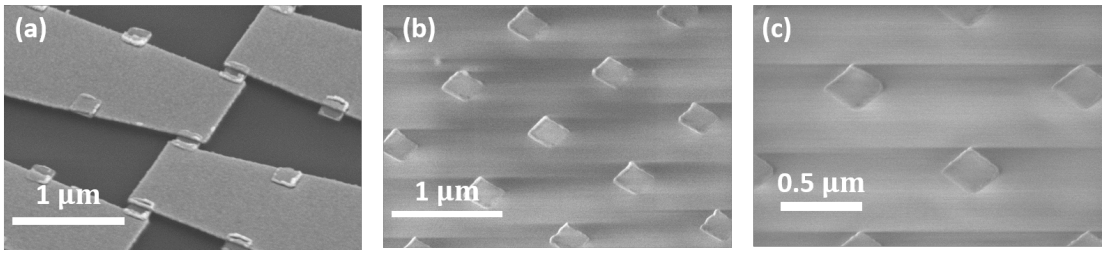

Figure 3.5: SEM images showing dots deposited under different sputter pressures, and with the inclusion of a side-mill step. Dots in (a) were deposited at an argon pressure of 3.0 mTorr, while dots in (b) were deposited at 1.5 mTorr, with all the same paramaters otherwise. (The inclusion of the gold contacts in (a) not in (b) is incidental and unimportant for our discussion here). Dots in (a) display both a larger amount of fencing on each dot (seen as the white edge around dots) than (b), and fencing that generally is around the full perimeter of the dot. In (b) the fencing is markedly decreased, and the increased directionality of the low-pressure sputtering step is evidenced from fencing appearing only on two sides of the dot; this is due to the Ru gun being tilted to the normal of the sample during deposition. A 90 s ion mill step at 15° to the substrate plane removes nearly all the fencing from the dot, as illustrated in (c). Apparent streaks in (b) and (c) are artifacts of the SEM imaging process and are not part of the sample itself.

angle near the normal of the chip to remove any oxide layer on the top of the dots, and then is rushed to the deposition chamber to deposit the contacts; in general, the dots are only in atmosphere for about 20 s between leaving the ion mill and pumping down in the deposition chamber. The final result is illustrated in fig. 3.4(f).

3.1.6 Material Deposition

Two different methods of material deposition were used in this work: thermal evaporation and DC sputtering. Thermal evaporation is achieved by heating material under vacuum until evaporation; material then diffuses through the chamber until eventually reaching the substrate, where it condenses and coats the substrate. The material is heated either by a high-current electron beam directed through the material, or by joule heating of a crucible containing the desired material. The directional nature of the vapor diffusion makes evaporation a very high resolution technique. However, evaporation has two major shortcomings. Evaporation of alloyed materials may not preserve the desired

stoichiometry if constituent materials evaporate at different rates for a given temperature. In principle this can be overcome by codeposition of the elemental constituents of the desired alloy; this option was not available for this work, however. Evaporation can also be problematic when depositing materials with high evaporation temperatures like tungsten, as the high-energy evaporated molecules can can both damage resist edges on impact, reducing resolution, and can also end up "hard-baking" resist, making liftoff much more difficult.

In contrast, sputtering is a "cold" process achieved by accelerating ionized argon molecules into a target of the desired material. A small partial pressure of argon is bled into the vacuum chamber, and a high voltage between the target and a cathode ionizes the argon. An arrangement of permanent magnets contains the plasma, and when the ions hit the target, the kinetic energy of the argon causes amounts of the target to sublime from the surface. These high energy particles quickly thermalize with the surrounding argon gas, avoiding the high-energy problem seen in evaporation. In addition, constituent elements of alloys will tend to sublime at the same rate. However, the thermalization of the sputtered material with the gas also means that nearly all directionality of the deposition is lost, and so sputtering tends to lead to lower resolution, and is more likely to result in fencing. To avoid fencing as much as possible from sputtering deposition steps, depositions were performed at the lowest argon pressures at which a sputtering plasma could still be struck. By keeping the argon molecule density low, sputtered particles undergo fewer collisions on the way to depositing on the substrate, conserving some amount of directionality and leading to less fencing; the difference between a high- and low-pressure deposition is illustrated in fig. 3.5(a)-(b). In principle, this parameter choice is a tradeoff for depositing a less uniform film–in practice we do not observe any notable differences in material properties.

In this work, the intial photolithographically patterned wafers are coated by thermal evaporation of Ti and Au in a CHA Industries electron beam evaporator in the MNC, while both the magnetic structures and the fine contacts of W and Au were deposited by DC sputtering. The contacts were deposited by an AJA deposition system in the MNC, and the magnetic dots were deposited in our lab's in-house sputtering system.

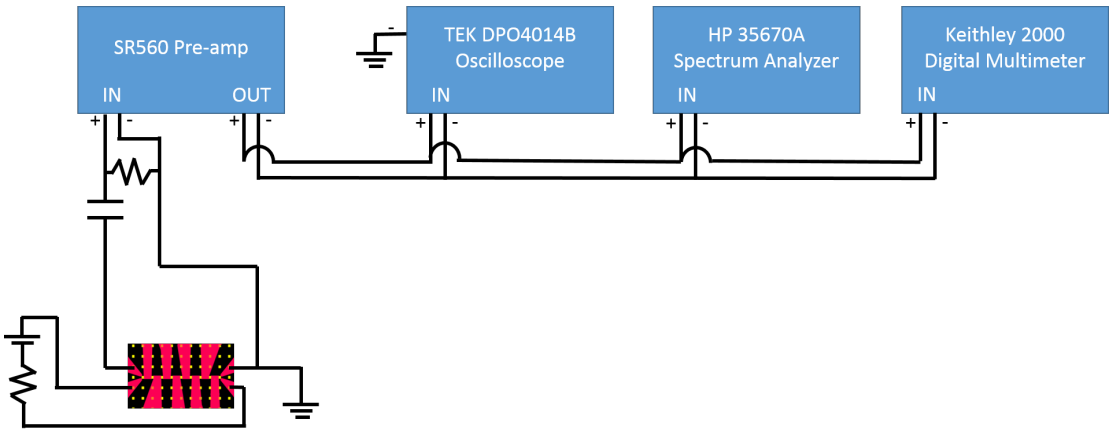

Figure 3.6: A cartoon picture of the measurement apparatus. The current is sourced through the full chain of dots by a battery-powered source shown in the lower left. The sample is grounded on the negative voltage measurement pin, and then the voltage signal is sent through a passive high-pass filter to buck out any DC signal before being amplified by the SR560 pre-amp. The amplifed signal is then sent to several measurement devices. We note that the - pin of the input and output of the SR560 are tied together, effectively propagating the ground provided to the sample on the V- pin of the measurement to the - inputs of all the measurement equipment shown. The DPO4014b also provides an explicit ground to its - pin, creating a ground loop. We find that this ground loop does not appreciably affect the measurement.

3.2 Measurement Apparatus

The measurement apparatus allows for DC resistance measurements to be made on samples under an applied magnetic field. A cartoon picture of the setup is shown in fig. 3.6. Two pairs of parallel-connected 1.5-volt AA batteries are placed in series with a low-noise metal film resistor, and then with the sample to source current. The resistor is chosen such that source current is typically $\sim$300 μA, the maximum value of current we find does not cause irreversable effects in the samples; samples have been able to withstand up to 1 mA of source current without failure, but irreversible degradation of magnetic properties are observed at currents higher than 300 μA, presumably due to electromigration between the electrode seed layer and the Py dot (see, for example, Ref. [40]). Low-noise Beldin Belfoil shielded twisted-pair cable connects the current source to the the breakout box.

Voltage signals are amplified by an Stanford Research 560 pre-amplifier (gain=200),

followed by a Tektronix DPO4014b real-time oscilloscope to record time records, a Hewlett-Packard 35670a spectrum analyzer to record voltage spectra. Since the RTN signal of interest typically is floating on top of a large DC voltage signal (especially on measurements of chains of many dots), the signal is sent through a passive high-pass filter with time constant $RC \approxeq 2$ s to AC-couple the signal before reaching the pre-amp to prevent DC overloading. If only a single dot is being measured, however, DC voltages are small enough that the high-pass filter is not necessary. In this case, the output voltage is sometimes also fed to a Keithley 2000 multimeter set in voltmeter mode to record sample resistance vs. field.

The applied field is generated by either four Leybold 562 13 electromagnets mounted around a U-shaped piece of soft iron, with the sample sitting in the gap, or a handmade Helmholtz coil, with the sample in the center of the coils. Current is sourced through the electromagnet by a Kepco BOP 50-2M in constant-current mode, and is controlled via an external programming voltage provided by the auxillary output of a Stanford Research 830 lock-in amplifier.

The SR830 and HP35670a both communicate with a PC via IEEE-488.2 GPIB communication to both save data and to control the equipment; we use a National Instruments USB-GPIB-HS+ controller to achieve this. The DPO4014b transmits its data via USB connection. Direct USB connection of the PC to the measurement equipment, however, both introduces ground loops, and otherwise contaminates the clean instrument ground with both the dirty ground on the PC, and extraneous digital noise from PC processes (see section 3.3 for more information on grounds). To mitigate this, the USB-GPIB converter and DPO4014b are both run through a B&B Electronics UHR304 USB opto-isolation hub before the signal is sent to the PC. We note that the UHR304 internally configures itself to run either as a high-speed or full-speed USB hub (with the odd naming convention of high-speed being faster than full-speed), contingent on what equipment is plugged into it. Both the USB-GPIB controller and the DPO4014b need to run in a high-speed configuration to avoid communication errors; however, it seems the opto-isolator will sometimes mistakenly configure itself as a full-speed hub depending on the order that equipment is plugged in. Our best solution for avoiding this error, unfortunately, has been to try different permutations of unplugging and replugging USB connections until communications are functional–a more repeatably consistent method

has not yet been devised.

3.2.1 Sample Preparation

Before samples can be measured, electrical connection to the sample must be made via aluminum wire bonds. Sample chips are loaded into a Spectrum Semiconductor CSB02813 28-pin DIP chip carrier, secured to the chip carrier by a small amount of Apiezon N-grease to the back of the chip. The chip carrier is plugged into a custom breakout sample block, which allows toggling between measuring individual pins of the carrier and shorting all pins together. Aluminum wire bonds are made to connect the lithographically defined contact pads on the chip to the contact pads on the chip carrier, and then 2-terminal resistance measurements are made between individual pins using a Fluke Multimeter as a low-current Ohmmeter to ensure sample integrity before proceeding; with the Fluke manually set to a 10 kOhm measurement range, 10 μA of current is sourced, which is well within the safe limits for our dots. A single dot typically has a 2-terminal resistance of about 190 Ohms, and the full chain of nine dots has a resistance of about 500 Ohms.

To avoid electrostatic discharge (ESD) through samples, care is taken to have all electrical connections to the sample shorted together as often as possible when the sample is not being measured. This includes manually shorting all sample connections together by tall wire bonds to protect the sample when the chip carrier is moved from the sample block to the measurement apparatus. The tall bonds are easily removed by tweezers once the chip carrier is plugged in.

3.2.2 Sample Housing

A custom-made breakout-box receives the chip carrier to allow electrical contact to the wire bonded sites. 12-position rotational switches allow designation of any of the 12 wire bonded locations to be assigned to the I^+, I^-, V^+, and V^- pins in the four-terminal measurement. A dedicated ground connection to the breakout-box always holds the V^- pin at ground to protect the sample from transient voltages.

The breakout-box is mounted on a turntable with 0.5° resolution; with the sample between the poles of the electromagnet, this allows application of a angle-resolved

magnetic field.

3.3 Grounding

Since our aim is to measure a very small fluctuating voltage signal and analyze its spectral content, extreme care must be taken to ensure that any voltage background signals are as small as possible, so as to not obscure the signal of interest. In addition, our magnetic nanodots are extremely fragile to ESD; surge currents on the order of only 1 mA can cause dots to detonate, which corresponds to a voltage spike of only ~ 10 mV. Fortunately, both problems can be solved by judicious grounding of all equipment involved in the experiment, while being careful to avoid ground loops.

3.3.1 Ground Receptacles

The laboratory has three types of grounding receptacles available, as shown in fig. 3.7: "dirty" ground, "clean" or "orange" ground, and "instrument" or "green" ground. All ground pins on gray electrical receptacles are considered to be "dirty" grounds. These grounds should be used for any electrical appliances in the room that are not intended to be used in directly measuring a signal. Dirty grounds typically can have large transient voltages on them from the appliances connected to them, which at best will obscure voltages one intends to measure, and at worse can damage of dots from the large transients.

Orange ground similarly comes from the ground pin of orange electrical receptacles in the lab. Nominally, the orange ground is isolated from the dirty ground and is cleaner–in practice this isolation does not appear to be particularly robust, as small ESD surges on the orange ground have caused sample failure when the sample is inadverdantly connected to dirty ground. Our convention is to treat the orange ground as a separate ground connection than dirty ground, and to use the orange ground as reference ground for experimenting on more robust samples where PSD measurements are not needed; obviously, however, the actual level of isolation of orange ground from dirty is in question, and all sensitive applications should use instrument ground instead.

Instrument ground is acquired from the green banana cable connections along the wall. Each instrument ground receptacle has a dedicated connection via an AWG-000

Figure 3.7: The three types of grounding receptacles available in the lab. The dirty ground shown in (a) is used for all equipment not in direct electrical contact with the sample, so as to protect the sample from surges on the line and to avoid contaminating the noise floor. The orange or "clean" ground shown in (b) is used only to ground the experimenter in this work, as its isolation from dirty ground is not sufficient for other uses. All equipment involved in direct measurement of voltages in the experiment is connected to the instrument ground in (c). Instrument ground is also used to ground the sample itself to protect from transients, which can cause sample failure.

cable to a large busbar which all instrument grounds on the floor connect to. This busbar then connects directly to the Ufer ground for the building. This electrical isolation from all other grounds and direct connection to the watertable through Ufer ground ensures that the instrument ground is the most electrically quiet ground available, and thus is the preffered choice of ground for all connections associated with the measurement.

It should be noted, however, that since different instrument grounds on the same floor are not isolated from each other, improper use of instrument ground in one location can affect all other instrument grounds on the same floor of the building. This includes "contamination" of instrument ground by electrical contact to either of the other ground connections. Care should be taken from the outset to avoid this problem, as diagnosing it is rather difficult; since all ground receptacles eventually connect to earth ground through a very low impedence, electrical connectivity tests will not reveal whether grounds are crossed this way or not, and one must rely on visual inspection to find such crossings. Failure to avoid crossing grounds will at best lead to extraneous noise peaks in PSD measurements (especially at 60 Hz and its harmonics), and at worst will result in sample failure due to voltage surges on the dirty or orange ground.

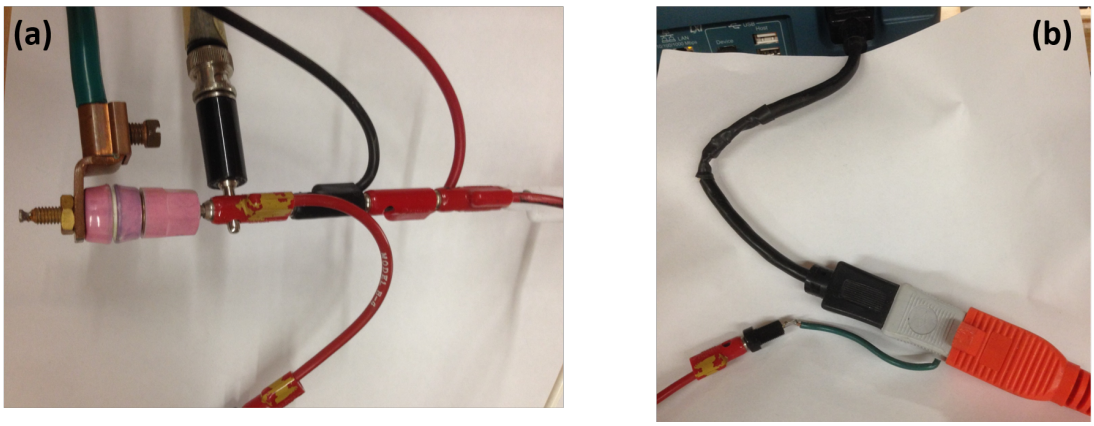

Figure 3.8: Photos of instrument ground branching at the experimental setup. In (a), instrument ground enters through the green cable at top-right and then branches off to each location requiring instrument ground. Banana cables are the preferred method of propagating ground; the single BNC is being exploited only for its length in lieu of a long banana cable for one particular connection. Ideally, all equipment powered by wall voltage would receive their ground as in (b) (ground enters the frame in the lower-left), with a grounding connection spliced in as close to the branch point as possible.

3.3.2 Powering and grounding of equipment

Instrument ground is brought to the experimental setup by a AWG-6 multistrand copper cable. As near as possible to all the equipment, the cable is connected mechanically via clamping mechanism to a banana receptacle, from which all ground connections to equipment branch, with one connection spliced into a power strip to provide a ground connection to electronic equpiment, and a dedicated branch for each other desired ground connection–this branch point is shown in fig. 3.8(a). Ideally, secondary branching such as that at the power strip will not occur to ensure that all pieces of equipment are at as close to the same potential as possible; the most meticulous method of grounding of experimental equpiment would involve splicing a dedicated ground branch into the power cable powering a given piece of equipment as close to the equipment as possible. In practice, however, we find that allowing one additional branching connection at the power strip does not appreciably degrade any signals; the only piece of electronic equpiment recieving its own dedicated ground branch is the Tektronix oscilloscope. This is done to elminate transient 60 Hz noise, and the connection is shown in fig. 3.8(b).

Banana cables are used at the branch point as they were found to have the lowest pickup and impedence while still remaining practical for making connections to equipment–in some iterations of the experiment, the central conductor on BNC cables was used to propagate ground to some locations. However, capacitive pickup between the BNC center conductor and shielding produced unwanted noise peaks in the 10 kHz to 100 kHz range. A single BNC cable remains in the finale iteration of the experiment as a matter of convenience–ground must be propagated a significant distance to ground the power strip powering most equipment, and a banana cable of suitable length was not available. Use of this BNC cable does not appear to add noise peaks, however.

High-current power supplies and experimental PCs used to communicate with equipment should *not* be connected to the instrument ground; both should instead be grounded by dirty ground. Power surges on the power supplies can easily destroy grounded samples, and digital processes on computers can dirty a ground connection and add many unwanted peaks to the PSD. As noted in section 3.2, a USB isolation hub still allows measurement equipment at instrument ground to connect to a PC with a dirty ground connection while avoiding contamination and ground loops.

A final note on grounding is that, as noted above, none of the three ground connections are fully isolated from each other, and as such, significant ground surges on any ground line can affect any other ground line if the surge is large enough. In particular, we have observed failure of dots under measurement (with one end connected to instrument ground, as mentioned in section 3.2.2) concurrent with powering on or off dirty-grounded Kepco power supplies elsewhere in the lab. Best practices dictate that no high-current or high-voltage power supplies should be powered on or off without first ensuring that all dots are shorted to instrument ground for protection.

3.3.3 Grounding of Experimenter

The experimenter also needs to take care to be appropriately grounded, so as to not damage samples by ESD. A Statshield brand ESD coat is worn during all wire bonding, experimental setup, and measurement to protect the sample. We note that the coat is connected to orange ground rather than instrument ground; this ensures that any large transients created from ESD sinking through the coat do not come close to the sample and instead are safely sunk away through an isolated path. Iterations of the experiment

where the experimenter was connected to instrument ground saw frequent sample failure correlated with the experimenter standing up or otherwise shifting position; switching the experimenter to orange ground eliminated this problem.

Chapter 4

Results

We first present a brief discussion of characterization of the individual dots before moving on to results of aggregate systems.

4.1 Anisotropy and RTN behavior in dots

Individual dots' energy barriers can be characterized by making measurements of easy axis coercivity H_C [32] through the AMR. Briefly, if a field is applied along the easy axis of the dot, the magnetization of the dot should switch when the well the magnetization sits in becomes inverted; that is, when $\frac{\partial^2 E}{\partial \theta^2} = 0$ for $\phi = 0$. Using eq. (2.24),

$$\begin{aligned} 0 &= \left.\frac{\partial^2 E}{\partial \theta^2}\right|_{\phi=0,\theta=0} \\ &= \left. 8E_A \cos(4\theta) + mH_C \cos(\theta - \phi)\right|_{\phi=0,\theta=0} \\ &= 8E_A + mH_C \end{aligned} \tag{4.1}$$

Solving eq. (4.1) for E_A gives

$$E_A = \frac{mH_C}{8} \tag{4.2}$$

Using the standard magnetization value of 800 emu/cm^3 for Py and the geometry of the dot, we can calculate the dot's moment m, and thus can determine the dot's energy barrier height through coercivity measurements. On axis-field sweeps will show large

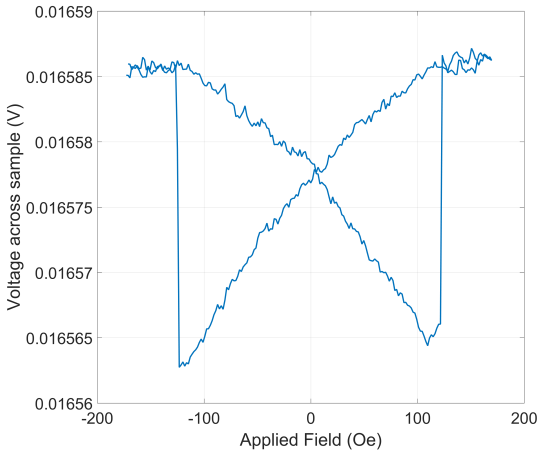

Figure 4.1: Voltage vs. applied field data for the field applied along the easy axis of the dot. At a max applied field, the magnetization of the dot is nearly uniform and gives and extreme resistance value, and hence a voltage extremum. As the field is swept, the dot magnetization relaxes to the zero-field configurational state as discussed in section 2.3.5, and as the field continues past zero, the magnetization continues to bend into a tighter C-shape to minimize the Zeeman energy. Eventually, the increase in exchange energy due to the magnetization bending becomes larger than the Zeeman energy, and the net magnetization direction flips, which is seen as the large jump in voltage in the plot. The field at which this jump occurs is defined as the coercive field H_C.

jumps in the AMR at the coercive field when the magnetization switches; an example is shown in fig. 4.1. Typical barrier heights for our dots are between 3 eV and 4 eV, which is in good agreement with measurements of 250 nm dots in [32].

Application of fields at 45° to the diagonal shows the activated switching behavior previously observed in ref. [34]. Time records display two state switching, and the corresponding PSDs show a Lorentzian lineshape, with the average switching time τ_r decreasing for increasing field values; an example is shown in fig. 4.2. These observations indicate that our modified contact geometry (as compared to ref. [34]) does not affect the dots' magnetic behavior.

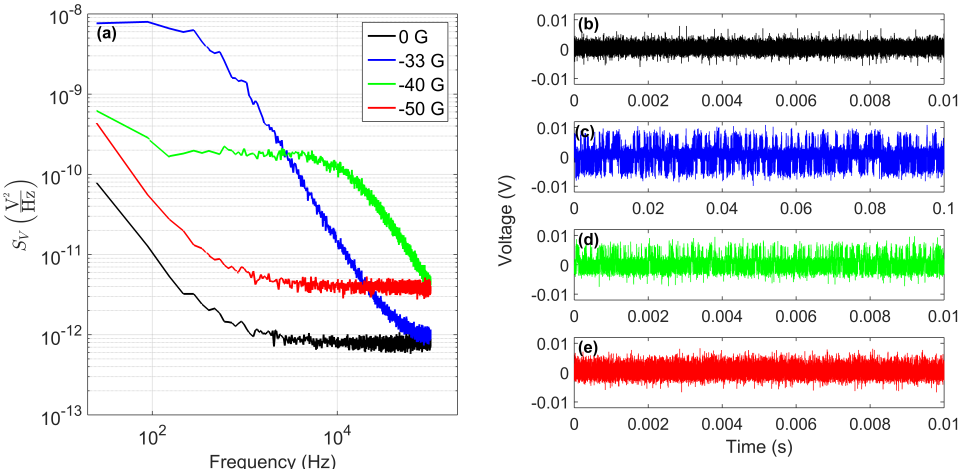

Figure 4.2: Voltage vs. Time and PSD vs. frequency are shown for a single dot for a magnetic field applied at an angle of 44° at various fields strengths. PSDs for four different field strengths are shown in (a), with color coded time records shown in (b)-(e). As the field strength increases from (b) to (e), the average relaxation time τ_r decreases (note the time scale difference between time record plots). This is also seen in the PSD data, where the rolloff frequencies $f_0 = \tau_r^{-1}$ increase with increasing field magnitude, with the rolloff frequency at -50 G exceeding the max frequency of the measurement, leading to its PSD appearing only as a raised noise floor.

4.2 Observation of $^1/_f$ noise in chains of dots

4.2.1 $^1/_f$ noise in chains of many dots

By connecting multiple chains of dots using wire bonds, we are able to create "macrochains" of up to 81 dots. Application of fields of between 40 and 60 Oe at 45° to the chip edge consistently shows $\frac{1}{f}$ noise in macrochains of dots. An example of $\frac{1}{f}$ noise in a macrochain of 36 dots is shown in fig. 4.3. We note that despite there being upwards of 30 dots in a given macrochain, only around 10-20% of dots show RTN at any given choice of (H, ϕ), so the emergence of $\frac{1}{f}$ noise in any given macrochain is likely only due to a handful of RTN signals. This is supported by the PSDs and time records of the individual chains of dots, which typically show either a single RTN signal time record and a Lorentzian PSD, or, less frequently a time record showing two RTN signals at different characteristic frequencies, and a PSD to reflect that. An example of both the former and latter are shown in figs 4.3(b) and (c), respectively, with corresponding PSDs

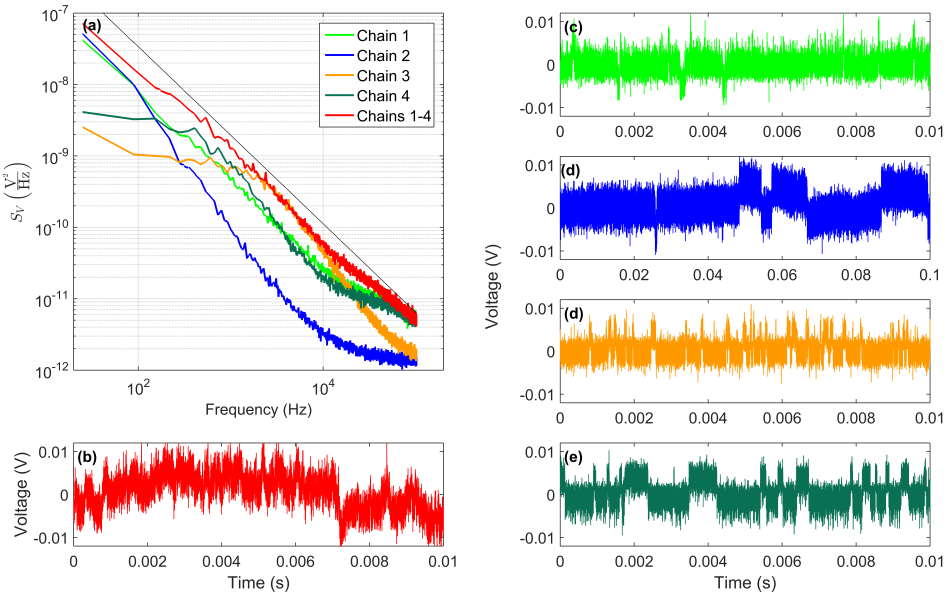

Figure 4.3: PSD and time records of four different chains of dots on a single chip, as well as for all four chains jumped together. Time records of individual chains (b)-(e) show clear RTN signals from either one or two dots in a given chain. (c) and (d) show only a single RTN signal, which is reflected in the corresponding PSDs in (a) having obvious Lorentzian lineshapes, especially at low frequencies where the $S_V \propto f^{-2}$. (b) and (e) both show both a very high frequency RTN component, and a lower one, giving the composite PSD lineshapes shown in (a). (f) shows the composite time record measured across all four areas, with a clear $\frac{1}{f}$ PSD in (a) for three decades of frequency space. A reference line drawn at a slope of $\frac{1}{f}$ is included in (a). The slow decay of the signal after jumps in (d) is due to dwell times approaching the RC time of the hi-pass filter mentioned in section 3.2.

shown in fig. 4.3(a).

We observe macrochain $\frac{1}{f}$ noise like that in fig. 4.3 in six samples fabricated under the same conditions, typically at applied field magnitudes around 40 Oe. An additional series of three samples fabricated under slightly different conditions show $\frac{1}{f}$ noise at applied fields around 55 Oe. A more detailed discussion of field strength distributions can be found in section 4.2.2.

4.2.2 Comparison to Van der Ziel model

As noted in sections 2.2.5 and 2.4, the Van der Ziel model predicts that for a constant distribution of barrier heights ΔE, a collection of activated processes will have a $\frac{1}{f}$ PSD. To determine if our system meets this criterion, we examine the distribution of ΔE's we expect from eq. (2.22). By combining eq. (2.22) with eq. (4.2), we can express the barrier height in terms of the applied field, which we now label as H_N to denote the applied field at which $\frac{1}{f}$ noise is observed, and the easy axis coercivity H_C:

$$\Delta E = \frac{mH_C}{8} - mH_N\left(\frac{2-\sqrt{2}}{2}\right). \tag{4.3}$$

If we want to observe $\frac{1}{f}$ noise over a bandwidth of 10 Hz $\leq f \leq$ 1 100kHz, we will need activated processes with the required distribution of relaxation times τ_r over a minimum range corresponding to this bandwidth [7]; to be safe, to achieve the aforementioned bandwidth, we will posit that we need an additional order of magnitude of τ_r's obeying this distribution (see fig. 2.2 for reference). Thus we consider systems with relaxation times in the range 1 s $\geq \tau_r \geq 10^{-6}$ s.

By inverting eq. (2.18), we can translate this range of τ_r's into a corresponding range of ΔE's:

$$\Delta E = k_B T \ln\left(\frac{\tau_r}{\tau_0}\right), \tag{4.4}$$

where τ_r once again ranges from 10^{-6} s to 1 s. It is over this range which we require ΔE to have a flat distribution. From eq. (4.3) then, for a fixed applied field H_N we require a flat distribution of H_C's; that is,

$$g(H_C)\ \mathrm{d}H_C = C\ \mathrm{d}H_C \tag{4.5}$$

where C is a constant. We note that the range over which eq. (4.5) must be true to satisfy our $\frac{1}{f}$ noise condition will vary as a function of applied field H_N, since ΔE also depends on H_N. So we consider the *range* of H_C's over which eq. (4.5) must hold to be a function of H_N.

To understand this functional range, we combine eqs 4.3 and 4.4 to get:

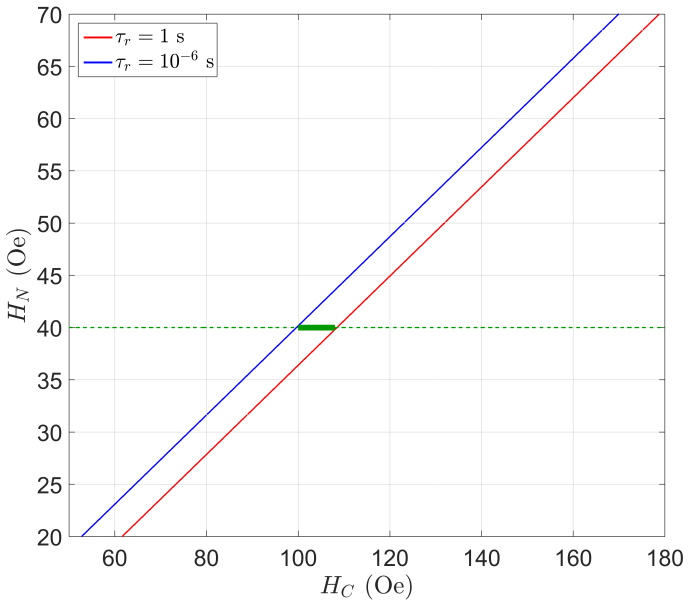

Figure 4.4: Plot of eq. (4.6) for $\tau_r = 1$ s and $\tau_r = 10^{-6}$ s. For a given distribution of dots to show $\frac{1}{f}$ noise at a given applied field H_0, the locations where the two lines intersect $H_N = H_0$ give the values of H_C between which the distribution of H_C's must be flat. The plot implies that $g(H_C)\ \mathrm{d}H_C$ must be flat over minimum range of ~ 8 Oe to observe $\frac{1}{f}$ noise at one applied field value. For example, to observer $\frac{1}{f}$ noise at an applied field of 40 Oe, $g(H_C)\ \mathrm{d}H_C$ needs to be flat from 100 Oe to 108 Oe, illustrated by the thick green line. If $g(H_C)\ \mathrm{d}H_C$ is flat over a larger range than this, $\frac{1}{f}$ noise should be observed over an increasing range of H_N's.

$$H_C = \frac{8k_BT}{m} \ln\left(\frac{\tau_r}{\tau_0}\right) + 8H_N\left(\frac{2-\sqrt{2}}{2}\right). \tag{4.6}$$

If we choose a standard attempt time of $\tau_0 = 10^{-11}$ s, inputting the limits on τ_r mentioned above into eq. (4.6) will give the range of H_C's over which eq. (4.5) must hold. This is most easily visualized in fig. 4.4, where we invert eq. (4.6) to plot H_N as a function of H_C for both limits on τ_r. A horizontal cut of this plot at a given value of H_N shows the range of H_C's needed to satisfy the noise condition at an applied field H_N.

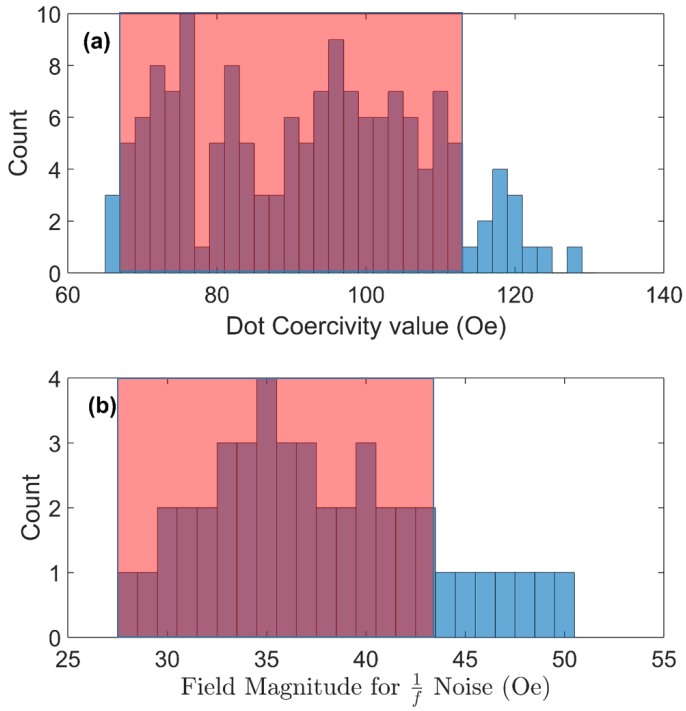

Figure 4.5: Histograms showing the easy axis coercive field H_C for $\sim$ 100 Py dots (a), and applied field magnitudes H_N where $\frac{1}{f}$ is observed in macrochains of dots (b). Coercivity measurements were taken along both easy axes for a given square dot, with both coercivities contributing individual points to (a). The shaded region of (a) where the distribution of H_C's are approximately constant correspond to a predicted range of H_N's denoted by the shaded region in (b).

Data from a series of six samples fabricated under identical conditions is shown in fig. 4.5 as a histogram of both individual dot coercivities, and of applied fields where $\frac{1}{f}$ noise was observed. In fig. 4.5(a), the shaded region denotes a range of approximately constant distribution of H_C's, which predicts of a range of H_N's denoted by the shaded region in fig. 4.5(b). We observe close agreement between the shaded region in fig. 4.5(b) and the measured distribution of H_N's.

A second series of three samples whose dots were deposited under slightly different conditions give an overall shift in the average coercivity, as shown in fig. 4.6(a). With

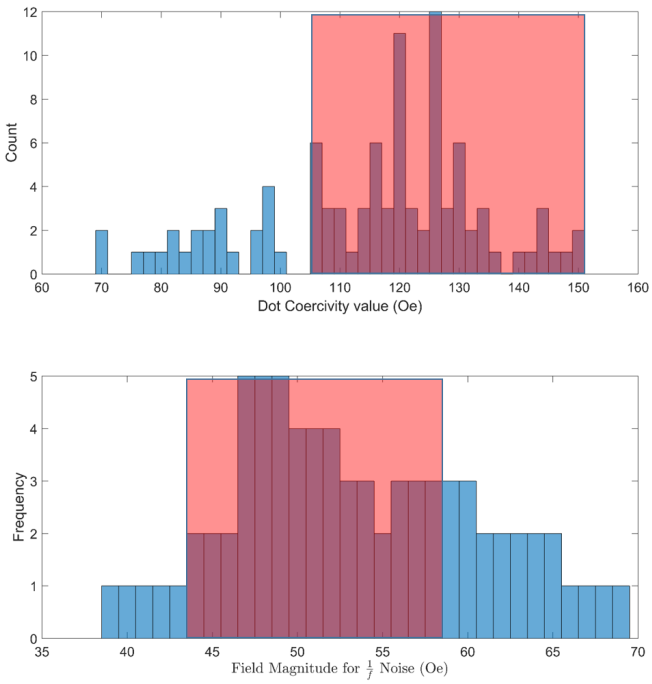

Figure 4.6: Histograms of dot coercivity and $\frac{1}{f}$ noise fields for a second set of samples.

fewer samples in the data set, the histogram is less uniform and so any conclusions we draw from this data will be less quantitative, but the region resembling a flat distribution of coercivities in fig. 4.6(a) again predicts a range of H_N's that corresponds with the measured values shown in fig. 4.6(b). The data at least *suggests* quantitative agreement, and displays the qualitative prediction that collections of dots with larger coercivities should show $\frac{1}{f}$ noise at larger applied fields.

4.2.3 $1/f$ noise in few dots

While the Van der Ziel theory predicts $\frac{1}{f}$ noise arising from an *ensemble* of Lorentizans, we note the somewhat surprising observation that $\frac{1}{f}$ noise arises from as few as two RTN signals, dependent on the PSD magnitudes and corner frequencies. An example is

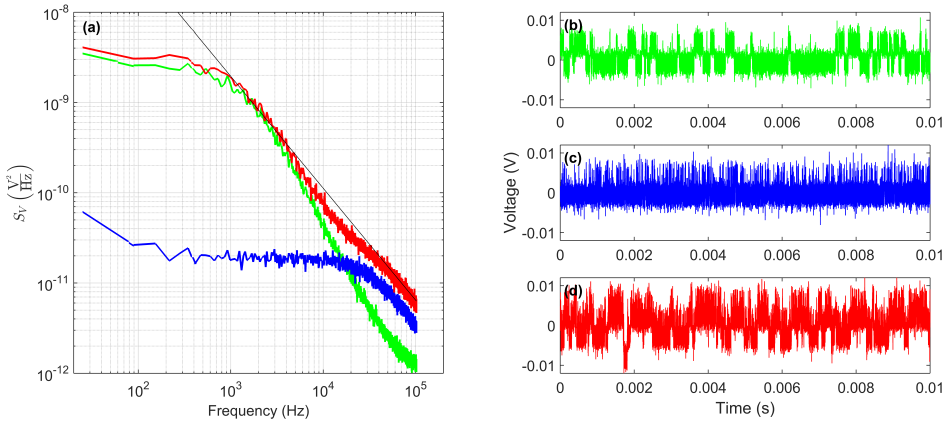

Figure 4.7: Time record and PSD of two individual dots, and their aggregate PSD showing $\frac{1}{f}$ noise. The individual time records in (b) and (c) show the clear RTN signals that combine in (d), but the combined PSD shown in (a) has a slope of $\sim \frac{1}{f}$ from $f \approx 10^3$ Hz to $f \approx 10^5$ Hz. A $\frac{1}{f}$ reference line is shown in black.

shown in fig. 4.7, where two individual dots with clear RTN time records and Lorentzian PSDs combine to produce a $\frac{1}{f}$ PSD for nearly two decades of frequency space. This result has been observed in five different pairs of dots, and shows the robustness of RTN signals leading to $\frac{1}{f}$ noise; while the formulation of the Van der Ziel theory assumes a continuum of signals, we have clear evidence that only a handful of signals are needed to acheive $\frac{1}{f}$.

4.2.4 Assumptions of the model

In our analysis, two major assumptions were made about the system. First, we assumed that the magnetization in a dot undergoing RTN is fully jumping between 0° and 90°. And second, in our energy analysis of the system, we assumed that all RTN signals had only one τ_r, so that the average duty cycle of a given signal was always 50%; this is equivalent to assuming that energy barriers are always symmetric.

The assumption that magnetization in dots jumps from 0° to 90° in all dots is certainly an oversimplification, since the Zeeman term in eq. (2.24) will move the location of the well minima away from 0° and 90° toward the dot diagonal, seen in fig. 4.8. This will alter our model in two ways–first, the height of the energy barrier ΔE will vary

from that calculated by eq. (4.3), which will alter τ_r of any given dot, and second, the magnitude of the RTN signal will decrease since the state will no longer be switching between maximum and minimum values of the AMR. Both these effects will have an impact on the effective distribution function $g(\tau_r)\ \mathrm{d}\tau_r$; the former effect for obvious reasons, and the latter because we have implicitly absorbed the magnitude of the RTN signal V_0^2 (see eq. (2.12)) into $g(\tau_r)$ under the assumption that it is constant for all dots. Since $g(\tau_r)$ is exponentially dependent on ΔE and only linearly dependent on V_0^2, we examine only the effect that the altered energy barriers will play since they will have the largest influence.

We procede by assuming a linear distribution of H_C's, and work back to determine the form of $g(\tau_r)$ this model gives, to compare to the desired form $g(\tau_r)\ \mathrm{d}\tau_r \propto \frac{\mathrm{d}\tau_r}{\tau_r}$.

To introduce $<90^\circ$ hopping, we fix the applied field H_N, and then alter eq. (2.25) to allow an arbitrary well location θ_0, written in terms of the dot coercivity H_C from eq. (4.2):

$$\begin{aligned}\Delta E =& E(\frac{\pi}{4}) - E(\theta_0) \\ =& (\frac{mH_C}{16} - mH_N) - \left(\frac{mH_C}{16}\cos(4\theta_0) - mH_N\cos\left(\theta_0 - \frac{\pi}{4}\right)\right)\end{aligned} \tag{4.7}$$

To determine $\theta_0(H_C)$, the location of the energy minima, we minimize the energy equation eq. (2.24) with $\phi = \frac{\pi}{4}$:

$$\left.\frac{\partial E}{\partial \theta}\right|_{\theta_0} = 0 = \frac{mH_C}{4}\sin(4\theta_0) + mH_N\sin(\theta_0 - \frac{\pi}{4}) \tag{4.8}$$

This transcendental equation can be solved numerically to determine $\theta_0(H_C)$, from which $\frac{\mathrm{d}\theta_0}{\mathrm{d}H_C}$ can also be calculated.

We next calculate the differential quantities $\mathrm{d}\tau_r$ and $\mathrm{d}\Delta E$ from eq. (2.18) and eq. (4.7) respectively:

$$\mathrm{d}\tau_r = \frac{\tau_0}{k_B T} e^{\Delta E/k_B T}\ \mathrm{d}\Delta E \tag{4.9}$$

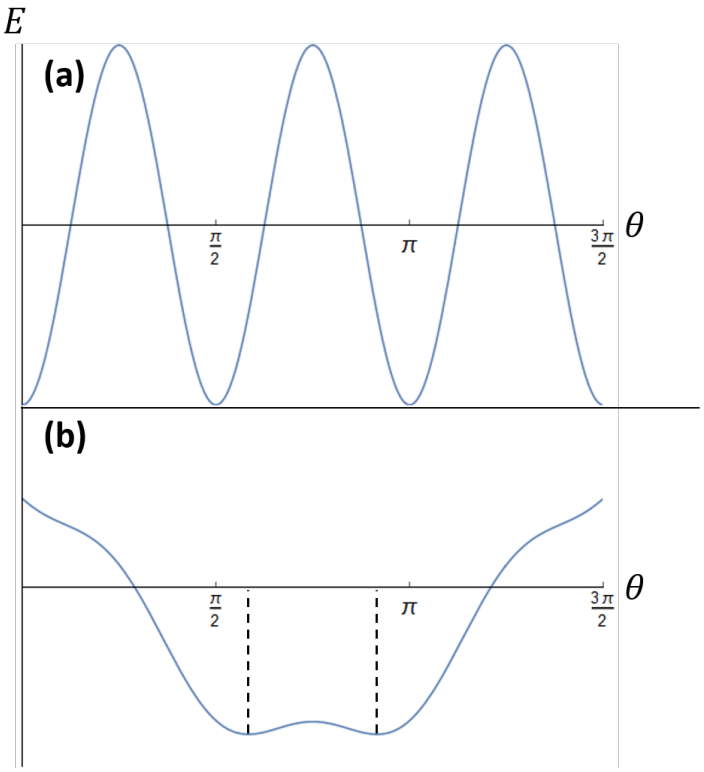

Figure 4.8: Plot of the energy landscape for both no applied field, and a strong field applied along the dot diagonal, calculated from eq. (2.24). Our model has assumed that energy minima remain at integer multiples of $\frac{\pi}{2}$ (that is, along the dot's edge) for all applied field values, as in (a). However, (b) shows that for strong applied fields, this is clearly not the case, as the minima both shift toward $\frac{\pi}{4}$, with the vertical dotted lines showing the approximate locations of the minima.

$$\mathrm{d}\Delta E = \frac{m\mathrm{d}H_C}{16} - \left(\frac{-m\mathrm{d}H_C}{16}\cos(4\theta_0)\frac{mH_C}{4}\sin(4\theta_0)\frac{\mathrm{d}\theta_0}{\mathrm{d}H_C}\mathrm{d}H_C + mH_N\sin(\theta_0 - \frac{\pi}{4})\frac{\mathrm{d}\theta_0}{\mathrm{d}H_C}\mathrm{d}H_C \right) \tag{4.10}$$

We substitute eq. (4.10) into eq. (4.9) and solve for $g(H_C)\ \mathrm{d}H_C = C\ \mathrm{d}H_C$ to determine $g(\tau_r)\ \mathrm{d}\tau_r$:

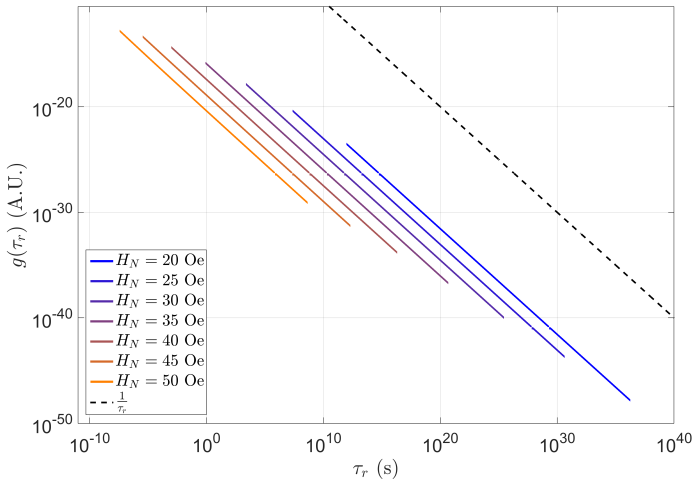

Figure 4.9: Plots of $g(\tau_r)$ for a constant $g(H_C)$ between 70 Oe and 110 Oe. Different lines correspond to different applied field strengths H_N; a vertical offset has been applied to each line for clarity. A dotted $\frac{1}{f}$ line is provided for reference. The slope of each line is indistinguishable from the $\frac{1}{f}$ reference, and applied fields in the 40-50 Oe range give the desired span of τ_r's for $\frac{1}{f}$ noise in the 10 Hz $< f <$ 100 kHz regime.

$$\frac{\tau_0 m}{k_B T} \mathrm{d}H_C = e^{\Delta E/k_B T}\left(\frac{1+\cos(4\theta_0)}{16} - \frac{H_C}{4}\sin(4\theta_0)\frac{\mathrm{d}\theta_0}{\mathrm{d}H_C} - H_N \sin(\theta_0 - \frac{\pi}{4})\frac{\mathrm{d}\theta_0}{\mathrm{d}H_C}\right)^{-1} \mathrm{d}\tau_r \tag{4.11}$$

With the RHS of eq. (4.11) giving a functional form of $g(\tau_r)\ \mathrm{d}\tau_r$, we plot $g(\tau_r)$ as a function of τ_r for a variety of applied fields H_N, with the assumption that $g(H_C)$ is constant between 70 and 110 Oe, the range of experimentally observed constant $g(H_C)$ in fig. 4.5(a). The result is plotted in fig. 4.9 for H_C ranging from 20 Oe to 50 Oe. We note two important features on this plot. First, the $\frac{1}{\tau_r}$ dependence appears to be preserved in this model, maintaining the functional form of $g(\tau_r)$ required by the Van der Ziel model to produce $\frac{1}{f}$ noise. Second, applied fields from 50 Oe down to $\sim$ 40 Oe give average switching times τ_r in the range 1 s $> \tau_r > 10^{-6}$ s as we require for $\frac{1}{f}$ noise in the 10 Hz $< f <$ 100 kHz range, which is in reasonable agreement with the region of

observed noise fields in fig. 4.5(b).

The second assumption made in our model is that the configurational anisotropy is truly symmetric about the dot diagonal, and that the applied field is always directly along this diagonal, leading to RTN signals with a 50% duty cycle. This assumption is obviously incorrect from looking at the time records of the data shown, with a range of duty cycles exhibited. The origin of this discrepency is likely the same fabrication imperfections that give a range of RTN frequencies at a given field; errors in a rectangualr dot's aspect ratio would lead to a uniaxial term added to the anisotropy, breaking the energy barrier symmetry about the dot corner, and errors in rotational alignment would lead to slightly rotated dots, resulting in a different diagonal-pointing angle for different dots. These sorts of discrepencies could alter the predicted RTN oscillation frequencies, which in principle could alter τ_r distributions and affect the observation of a $\frac{1}{f}$ PSD.

A quantitative analysis introducing uniaxial anisotropy and rotational shifts into our model is beyond the scope of our work, but we offer the following qualitative comments. While it is obvious that individual dots may display non-symmetric behavior, our statistical analysis of energy barriers in section 4.2.2 gives agreement with the theory despite the questionable symmetry assumption. Additionally, as noted in section 4.2.1, it appears that fewer than 10 oscillating dots are necessary in any individual system to achieve the $\frac{1}{f}$ signals seen, and this is further proven in section 4.2.3, where $\frac{1}{f}$ noise is observed for only a pair of RTN sources. This move from the Van der Ziel model's language of continua of Lorentzians and distribution functions to discrete (low) numbers of Lorentzians in individual experimental systems indicates that the emergence of $\frac{1}{f}$ signals from Lorentzians is more robust than a first glance at the continuum theory might suggest. Thus it is reasonable that a system resembling, but not identical to, the ideal Van der Ziel system could still display $\frac{1}{f}$ noise; the rigid conditions demanded by the Van der Ziel model are perhaps sufficient conditions for $\frac{1}{f}$, but not necessary ones.

Chapter 5

Conclusions and Future Work

5.1 Conclusions

The Van der Ziel theory of $\frac{1}{f}$ noise posits that $\frac{1}{f}$ noise can arise in systems with a distribution of Lorentzian power spectral densities that goes as the inverse of the characteristic roll-off times of the individual Lorentzians. In a systems described by thermally activated processes, this distribution of characteristic times is equivalent to a flat distribution of energy barriers. Using the four-fold symmetric configurational anisotropy model of square nanomagents developed by ref. [32], the Van der Ziel theory has been demonstrated by a ground-up approach, measuring both $\frac{1}{f}$ noise in the aggregate system, and the individual Lorentizan spectra of the constituent dots. The individual noise signals come from random telegraph noise oscillations of the dots' magnetizations, which are measured using the anisotropic magnetoresistance. A statistical analysis of multiple systems shows agreement between the predicted applied fields where noise should be observed, and the observed quantities. This analysis holds for a second set of samples with a different average energy barrier height.

The appearance of $\frac{1}{f}$ noise from Lorentzian spectra requires far fewer constituent Lorentzians than might be expected. Fewer than 10 dots undergoing RTN are necessary to observe $\frac{1}{f}$ over 3 decades of frequency space, and up to 2 decades of $\frac{1}{f}$ are seen from only two combined RTN signals, showing that this effect is rather robust; we observe $\frac{1}{f}$ noise arising even in low-n cases where the continuum description of the Van der Ziel theory is no longer applicable. The actual requirements on the distribution

of Lorentizans seems much looser than the Van der Ziel theory requires. This result indicates that in systems with any type of distribution of Lorentzian PSDs (be they from RTN signals, or otherwise), observation of $\frac{1}{f}$ noise is almost surely due to the combined Lorentzian signals.

5.2 Future Work

5.2.1 Magnetostatic coupling between dots

In this work, the spacing between the 250 nm permalloy dots was a constant 1 μm center-to-center. This large spacing was chosen to ensure that adjacent dots did not magnetostatically couple; however, lowering the spacing between dots should eventually allow such coupling to occur. It is not immediately obvious what effect such coupling might have on the emergence of $\frac{1}{f}$ noise in the dot ensembles; as the dot spacing goes to zero, the dots would presumably end up 100% correlated, destroying the $\frac{1}{f}$ signal as all the dots assumed the same time record, and the thus the same PSD. For intermediate spacings offering weak coupling, however, it is conceivable that the coupling might have an enhancement effect. A naive picture of two adjacent oscillating dots would have dot A seeing both the applied field H_A, and a small randomly changing field H_D from dot B. To first order, the fluctuating H_D could be viewed as only changing the magnitude of the field along the diagonal, which would cause dot B to see a variety of energy barriers ΔE, and thus oscillate with a variety of characteristic times τ_r. If dots can effectively offer a variety of RTN signals this way instead of just one, $\frac{1}{f}$ may be more easily achieved for even fewer dots.

An important measurement in this experiment would be confirming whether adjacent dots are truly coupling or not. In principle, a measurement resembling the ones in this work could be done, with a current running through a chain of dots, and time records being recorded simultanously of all the dots in the chain; correlation functions of the different signals would reveal whether coupling occurs. In principle, measurement of multiple dots simultanously seems simple; the Tektronix DPO4014b storage oscilloscope used in this work has four inputs, and TTL syncing of additional scopes could increase the number of possible measurements arbitrarily. However, the DPO4014b (and, to our knowledge, all commercially available storage oscilloscopes) explicitly grounds its

negative input pin, meaning that straightforward attempts to measure time records of multiple dots in a chain would result in multiple ground connections on the chain, nullifying most of the measurements.

A simple workaround to allow measurement of two dots at once is shown in fig. 5.1, where two dots sharing a common ground could be measured, with one time record requiring inversion before calculating a correlation function; it's not clear if the ground loop introduced into the system this way would introduce enough pickup to obscure the signals of interest, however. To measure more than two dots simutanously, outputs could be run through battery-powered optoisolators before the oscilloscope to avoid the grounding and ground-loop issues, or the measurement housing could be modified to facilitate use of a differential (A-B) input on the amplification stage.

5.2.2 $1/f$ noise in single dots

In addition to observing $\frac{1}{f}$ noise in collections of dots, $\frac{1}{f}$ was sometimes observed in a single dot, at applied fields higher than those that showed RTN. This effect was also observed by ref [41]. This phenomenon remains mostly unexplored; however, we offer several possible directions to begin understanding it.

The functional form of the configurational anisotropy in eq. (2.22) is simply a lowest-order approximation; the true energy landscape certainly has higher order terms. These higher order terms may afford a situation where the total energy landscape along the dot diagonal is approximately flat for certain applied field values, with multiple small local minima that the magnetization could hop between. The net AMR signal measured would be a superposition of RTN oscillators corresponding to each pair of wells, which in the aggregate could produce a $\frac{1}{f}$ signal. We note that this hypothesis does well at providing an explanation for high-frequency $\frac{1}{f}$ noise, but since the energy barriers involved would be rather small, the low-frequency RTN components necessary to build a $\frac{1}{f}$ spectrum at low-frequencies would not obviously be present in this picture.

The first step to testing this theory would be to better characterize the energy landscape of dots past the first order approximation given by eq. (2.22). Assuming an arbitrary configurational anisotropy $E_A(\theta)$, the new total energy of the system, and its derivative with respect to θ, are:

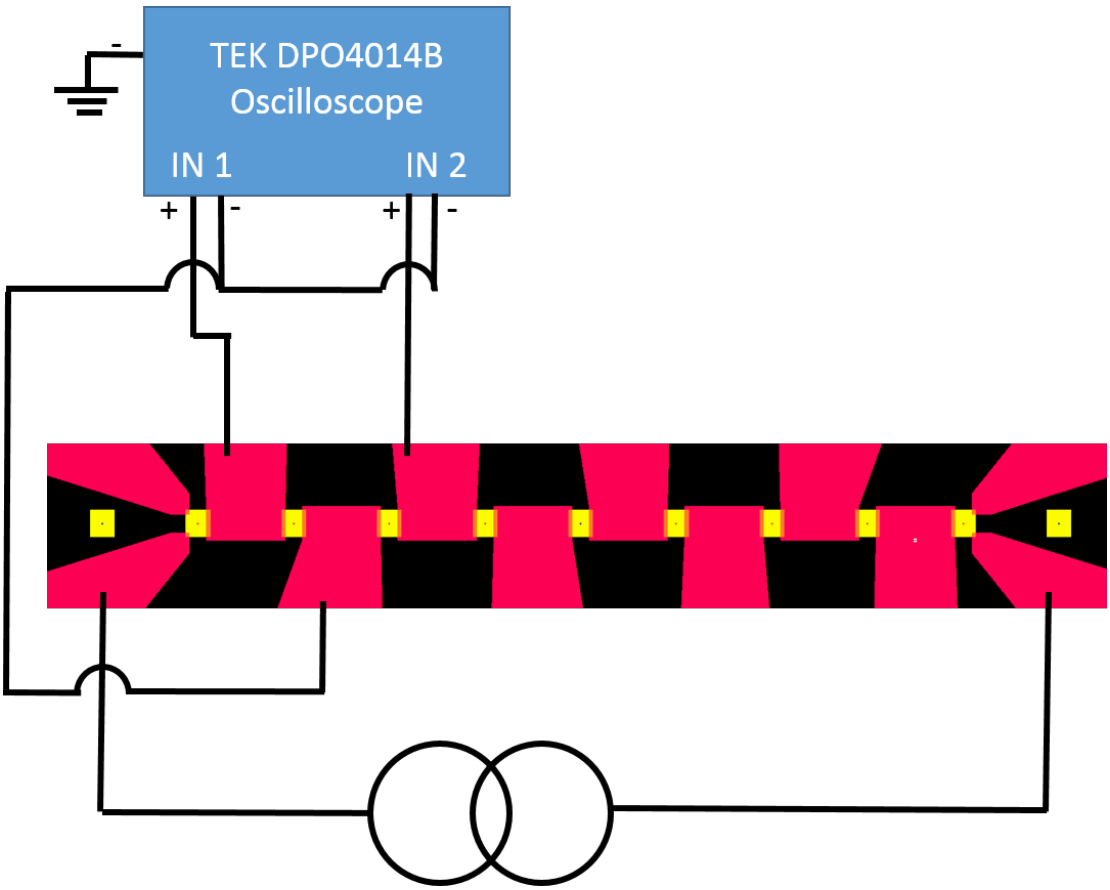

Figure 5.1: Cartoon of proposed measurement apparatus for measuring correlations between adjacent dots. The second and thirds dots from the left can be measured simultanously using the proposed setup. For the sake of clarilty, the amplification stages and filtering have been omitted, and the current source simplified in this picture.

$$E(\theta) = E_A(\theta) - mH\cos(\theta - \phi) \tag{5.1}$$

$$\frac{\partial E}{\partial \theta} = \frac{\partial E_A}{\partial \theta} + mH\sin(\theta - \phi) \tag{5.2}$$

A transport experiment similar those described in this work, but performed at low temperature, could determine θ with relatively high resolution through magnetoresistance values for a given applied field H at angle ϕ. Studies at low temperature should mitigate any hopping over energy barriers, and so all static magnetization measurements can be

assumed to be in a local energy minimum. Setting eq. (5.2) equal to zero would allow calculation of $\frac{\partial E_A}{\partial \theta}$, which could be used to reconstruct $E_A(\theta)$.

If necessary, a higher resolution measurement of the magnetization direction could be achieved by switching to either a giant magnetoresistance (GMR) [42] or tunneling magnetoresistance (TMR) [43] measurement, with the Py dot as one of the magnetic layers, and a magnetically pinned layer as the other. This switch would increase the angular resolution of the measurement by both increasing the signal magnitude (since ΔR between the minimum and maximum resistance states of both GMR and TMR can be orders of magnitude higher than AMR), and by switching to a magnetoresistive effect that has 2π symmetry, unlike AMR which has only π symmetry; the net dot magnetization direction would be uniquely determined by the resistance value in a GMR or TMR system. Care would need to be taken to ensure that the magnetic properties of the Py dot are not affected by the additional material in the GMR/TMR stack; recreation of the room temperature results of refs [32, 34] in the GMR/TMR system would be necessary before proceding with the low-temperature experiments suggested here.

It may also be that the Stoner-Wolfarth model of coherent rotation cannot describe the origins of this $\frac{1}{f}$ signal, and a switch to a more detailed microscopic picture is necessary. Micromagnetic simulations would likely be needed to inform experimental work moving in this direction.

References

[1] F. Reif, *Fundamentals of Statistical and Thermal Physics* (McGraw-Hill, New York, 1965).

[2] A. Ambrózy, *Electronic Noise* (McGraw-Hill, New York, 1982).

[3] J. Weber, Physical Review **94**, 211 (1954).

[4] S. Ekstein and N. Rostoker, Physical Review **100**, 1023 (1955).

[5] M. B. Weissman, Reviews of Modern Physics **60**, 537 (1988).

[6] P. Horowitz and W. Hill, *The Art of Electronics*, 2nd ed. (Cambridge University Press, New York, 1989).

[7] A. Van Der Ziel, Physica **16**, 359 (1950).

[8] A. Van Der Ziel, *Noise: Sources, Characterization, Measurement* (Prentice-Hall Inc., Englewood Cliffs, NJ, 1970).

[9] J. B. Johnson, Physical Review **32**, 97 (1928).

[10] H. Nyquist, Physical Review **32**, 110 (1928).

[11] D. Bell, 1/f Noise and Burst Noise, in *Noise and the Solid State*, chap. 2, pp. 35–56, Halsted Press, New York, 1985.

[12] S. Machlup, Journal of Applied Physics **25**, 341 (1954).

[13] P. Dutta and P. M. Horn, Reviews of Modern Physics **53**, 497 (1981).

[14] W. H. Press, Comments Astrophys. **7**, 103 (1978).

[15] T. Musha and M. Yamamoto, 1/f Fluctuations in Biological Systems, in *Proceedings of the 19th International Conference - IEEE/EMBS*, pp. 2692–2697, 1997.

[16] B. B. Mandelbrot and J. R. Wallis, Water Resources Research **5**, 321 (1969).

[17] F. G. Aliev *et al.*, Applied Physics Letters **91**, 43 (2007), 0803.3564.

[18] J. M. Almeida *et al.*, Journal of Applied Physics **99**, 26 (2006).

[19] A. Gokce, E. R. Nowak, S. H. Yang, and S. S. P. Parkin, Journal of Applied Physics **99** (2006).

[20] I. G. Sinai, Lorentz gas and random walks, in *Proceedings of Berlin Confrerence on Mathematical Problems in Theoretical Physics1*, pp. 12–14, Springer-Verlag, 1982.

[21] B. B. Mandelbrot and J. Ness, SIAM Review **10**, 422 (1968).

[22] H. Handel, Physical Review Letters **34**, 1492 (1975).

[23] M. A. Caloyannides, Journal of Applied Physics **45**, 307 (1974).

[24] I. Flinn, Nature **219**, 1356 (1968).

[25] P. Dutta, P. Dimon, and P. M. Horn, Physical Review Letters **43**, 646 (1979), arXiv:1011.1669v3.

[26] B. Cullity and C. Graham, *Introduction to Magnetic Materials*, 2nd ed. (John Wiley & Sons, Inc., Hoboken, NJ, 2009).

[27] R. O'Handley, *Modern Magnetic Materials: Principles and Applications* (Wiley-Interscience, 1999).

[28] J. D. Jackson, *Classical Electrodynamics*, 3rd ed. (John Wiley & Sons, Inc., Hoboken, NJ, 1999).

[29] M. E. Schabes and H. N. Bertram, Journal of Applied Physics **64**, 1347 (1988).

[30] R. Moskowitz and E. Della Torre, IEEE Transactions on Magnetics **2**, 739 (1966).

[31] R. P. Cowburn and M. E. Welland, Applied Physics Letters **72**, 2041 (1998).

[32] D. E. Endean, C. T. Weigelt, R. H. Victora, and E. D. Dahlberg, Applied Physics Letters **103**, 042409 (2013).

[33] E. Stoner and E. Wohlfarth, Philosophical Transactions of the Royal Society of London, Series A, Mathematical and Physical Sciences **240**, 74 (1948).

[34] D. E. Endean, C. T. Weigelt, R. H. Victora, and E. D. Dahlberg, Applied Physics Letters **104**, 252408 (2014).

[35] W. F. Brown, Physical Review **130**, 1677 (1963).

[36] T. McGuire and R. Potter, IEEE Transactions on Magnetics **MAG-11**, 1018 (1975).

[37] F. Guo, G. Mckusky, and E. D. Dahlberg, Applied Physics Letters **95**, 062512 (2009).

[38] F. Guo, G. Mckusky, and E. D. Dahlberg, Physical Review B **88**, 014409 (2013).

[39] M. Kitada, Thin Solid Films **131**, 21 (1985).

[40] M. Kitada, H. Yamamoto, and H. Tsuchiya, Thin Solid Films **122**, 73.

[41] D. E. Endean, *The Origin of Magnetic Noise in Nanoscale Square Dots Doctor of Philosophy*, PhD thesis, University of Minnesota, 2014.

[42] E. Y. Tsymbal and D. Pettifor, Solid State Physics **56**, 113 (2001).

[43] E. Y. Tsymbal, O. N. Mryasov, and P. R. Leclair, Journal of Physics: Condensed Matter **15**, R109 (2003).

[44] R. E. Williamson and H. F. Trotter, *Multivariable Mathematics*, 2nd ed. (Prentice-Hall Inc., Englewood Cliffs, NJ, 1979).

Appendix A

Derivation of PSD from Fourier Transform of Time Record

Suppose we have a real valued function $x(t)$ that is non-zero only for a specified region; that is

$$x(t) = \begin{cases} x(t), & -\frac{T}{2} \leq t \leq \frac{T}{2} \\ 0, & \text{elsewhere} \end{cases} \tag{A.1}$$

We can transform $x(t)$ into frequency space using a Fourier transform:

$$X(f) = \int_{\infty}^{-\infty} x(t) e^{-i\omega t} \, \mathrm{d}t = \int_{\frac{T}{2}}^{-\frac{T}{2}} x(t) e^{-i\omega t} \, \mathrm{d}t \tag{A.2}$$

Taking the absolute square of eq. (A.2) (and suppressing the argument of $X(f)$) gives

$$\begin{aligned} |X|^2 = X^* X &= \left[\int_{\frac{T}{2}}^{-\frac{T}{2}} x(t) e^{i\omega t} \, \mathrm{d}t \right] \left[\int_{\frac{T}{2}}^{-\frac{T}{2}} x(s) e^{-i\omega s} \, \mathrm{d}s \right] \\ &= \int_{\frac{T}{2}}^{-\frac{T}{2}} \int_{\frac{T}{2}}^{-\frac{T}{2}} x(t) x(s) e^{-i\omega(s-t)} \, \mathrm{d}s \, \mathrm{d}t \end{aligned} \tag{A.3}$$

If $x(t)$ is stochastic and stationary, we can consider an ensemble average to determine the expectation value of eq. (A.3) [1]:

$$\langle |X|^2 \rangle = \int_{\frac{T}{2}}^{-\frac{T}{2}} \int_{\frac{T}{2}}^{-\frac{T}{2}} \langle x(t)x(s) \rangle e^{-i\omega\tau} \, \mathrm{d}s \, \mathrm{d}t \tag{A.4}$$

If we let $s = t + \tau$, we have

$$\begin{aligned} \langle |X|^2 \rangle &= \int_{\frac{T}{2}}^{-\frac{T}{2}} \int_{\frac{T}{2}}^{-\frac{T}{2}} \langle x(t)x(t+\tau) \rangle e^{-i\omega\tau} \, \mathrm{d}s \, \mathrm{d}t \\ &= \int_{\frac{T}{2}}^{-\frac{T}{2}} \int_{\frac{T}{2}}^{-\frac{T}{2}} C_x(\tau) e^{-i\omega\tau} \, \mathrm{d}s \, \mathrm{d}t \end{aligned} \tag{A.5}$$

where $C_x(\tau)$ is the autocorrelation function of $x(t)$, as defined in eq. (2.1). In order to integrate eq. (A.5), we need to change variables to be able to integrate over τ. Using our susbstitution for s from above, we can choose to transform from $(t, s) \to (\tau, \eta)$ using

$$\begin{aligned} \tau &= s - t \\ \eta &= s + t \end{aligned} \tag{A.6}$$

Computing the Jacobian J (see, for example, Ref. [44]) gives $|J| = 2$, so

$$\langle |X|^2 \rangle = \frac{1}{2} \int_{\tau_1}^{\tau_2} \int_{\eta_1}^{\eta_2} C_x(\tau) e^{-i\omega\tau} \, \mathrm{d}\eta \, \mathrm{d}\tau \tag{A.7}$$

So it remains to determine the limits of integration for each integral by examining the integration domains pictured in fig. A.1. In eq. (A.7), we wish to integrate over η first, so we can set τ constant, and note in fig. A.1(b) that η ranges from $-T + |\tau|$ to $T - |\tau|$ for any given value of τ. This gives our limits on η. Now we can allow τ to run over its absolute limits in fig. A.1(b), giving us its limits of integration as $-T$ and T. Thus,

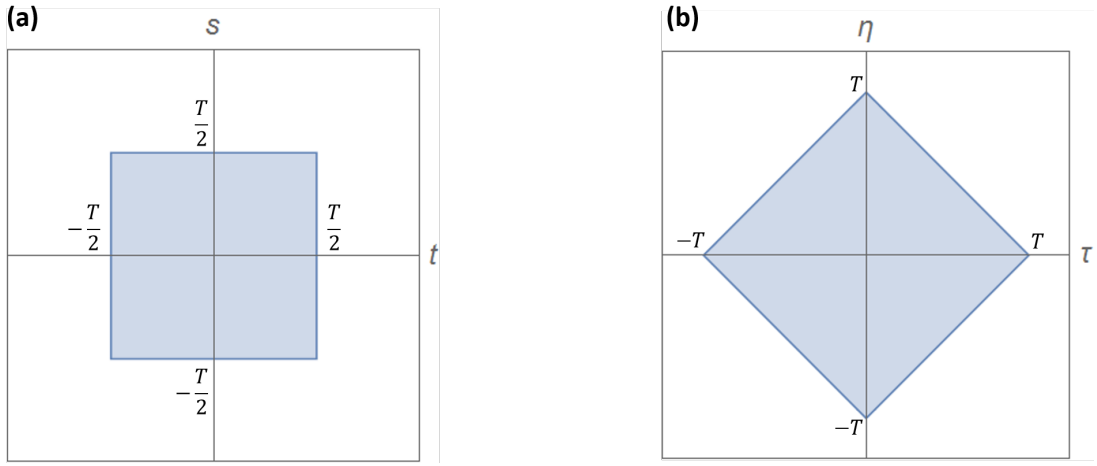

Figure A.1: Plots of domain of integration in both the original variables (s, t) in (a), and in the transformed variables (η, τ) in (b). Plot (b) is generated by transforming the limits of intetration from eq. (A.5) into the new set of variables using eq. (A.6).

$$\langle |X|^2 \rangle = \frac{1}{2} \int_{-T}^{T} \int_{-T+|\tau|}^{T-|\tau|} C_x(\tau) e^{-i\omega\tau} \, \mathrm{d}\eta \, \mathrm{d}\tau$$

$$= \int_{-T}^{T} (T - |\tau|) C_x(\tau) e^{-i\omega\tau} \, \mathrm{d}\tau \tag{A.8}$$

$$= T \int_{-T}^{T} \left(1 - \frac{|\tau|}{T}\right) C_x(\tau) e^{-i\omega\tau} \, \mathrm{d}\tau.$$

If we let $T \to \infty$, we can rearrange eq. (A.8) to write

$$\lim_{T\to\infty} \frac{\langle |X|^2 \rangle}{T} = \int_{-\infty}^{\infty} C_x(\tau) e^{-i\omega\tau} \equiv S_x(\omega) \tag{A.9}$$

as in eq. (2.2). Experimentally, this indicates that, for sufficiently long sample times T (that is, for $T >> \frac{1}{f}$ for all f in the band of interest), measuring the the average FFT of a signal is sufficient to determine its PSD.

Appendix B

Abbreviations

Table B.1: Acronyms

Acronym	Meaning
AMR	Anisotropic Magnetoresistance
CAD	Computer Assisted Drawing
CVD	Chemical Vapor Deposition
DIP	Dual In-Line Package
EBL	Electron-Beam Lithography
ESD	Electrostatic Discharge
GMR	Giant Magnetoresistance
GPIB	General Purpose Interface Bus
MIBK	Methyl Isobutyl Ketone
MNC	Minnesota Nanocenter
NMP	N-Methyl-2-Pyrrolidone
PC	Personal Computer
PMMA-CX	X% Resin of Poly(Methyl Methacrylate) in Chlorobenzene
PSD	Power Spectral Density
Py	Permalloy
RMS	Root-Mean-Square

Continued on next page

Table B.1 – continued from previous page

Acronym	Meaning
SEM	Scanning Electron Microscope
TMR	Tunneling Magnetoresistance
UHV	Ultra-High Vacuum
USB	Universal Serial Bus
UV	Ultraviolet
VSD	Voltage Spectral Density